ASSESSMENT OF OPTICAL TRANSMISSION AND IMAGE CONTRAST AT INFRARED WAVELENGTHS USING TISSUE SIMULATING PHANTOMS AND BIOLOGICAL TISSUES

By

KHUSHBU DIPAK PATEL

A thesis submitted to the

School of Graduate Studies

Rutgers, The State University of New Jersey

In partial fulfillment of the requirements

For the degree of

Master of Science

Graduate Program in Biomedical Engineering

Written under the direction of

Mark C. Pierce, Ph.D.

And approved by

_____

_____

_____

New Brunswick, New Jersey
October, 2017

ABSTRACT OF THE THESIS

Assessment of Optical Transmission and Image Contrast at Infrared Wavelengths using Tissue Simulating Phantoms and Biological Tissues

by **KHUSHBU DIPAK PATEL**
Thesis Director: Mark C. Pierce, Ph.D.

In vivo fluorescence imaging is an emerging technique with potential for usage in non-invasive cancer screening, surveillance, real-time surgical guidance, and staging. Fluorescence imaging uses the interaction of non-ionizing optical radiation with endogenous fluorophores or fluorescent labels to provide real-time wide-field images of tissue structure and/or functional components. When imaging *in vivo*, excitation light must travel through overlying tissue to reach the fluorescent target and emitted fluorescence must then propagate back through the overlying tissue in order to be imaged onto a camera. Recently, fluorescent contrast agents have been developed with excitation and emission wavelengths in the near infrared (NIR) spectrum (~700 – 1,000 nm) in order to minimize attenuation and maximize the measured signal from tissue.

While several clinical trials have shown the potential benefits of NIR contrast agents over visible fluorophores, there may still be room for improvement by moving to even longer wavelengths. As scattering is reduced as wavelength increases, some researchers are investigating fluorophores that emit in the short-wave infrared (SWIR) wavelength region (~1,000 – 2,300 nm).

This study focuses on examining optical transmission and image contrast at NIR wavelengths and SWIR wavelengths to determine which wavelength region may be optimal for development of fluorescent contrast agents. Transmission and contrast measurements were performed on both tissue simulating phantoms and real biological tissues using 780 nm, 980 nm, and 1550 nm wavelengths. From the experiments conducted, it appears that fluorophore emissions should be chosen based on the goals of the specific application. For an application that requires simple detection of signal, near infrared wavelengths will be better as they can be detected with higher signal levels. For an application that focuses on imaging fluorophore-labeled tissues, short-wave infrared wavelengths will be the better option as they provided better image contrast.

ACKNOWLEDGEMENTS

I would like to thank a few people without whom this would not have been possible. First, I would like to thank Dr. Pierce for his patience and advice throughout this entire process. He has been an amazing mentor from whom I have learned a lot throughout my years at Rutgers University, both undergraduate and graduate. I would also like to thank Dr. Hacihaliloglu and Dr. Najafizadeh for their suggestions and dedicating their time to being a part of my committee. I would like to thank my lab for their continued support and advice throughout my work.

I would like to thank my family and friends for their love, support, and encouragement, without which this would not have been possible.

Finally, Mummy and Daddy: thank you so much for being my pillar of strength since day one. Thank you for all the sacrifices you made so we could have a better education, I know it has not been easy.

TABLE OF CONTENTS

List of Figures

List of Tables

CHAPTER 1: INTRODUCTION

The goal of this thesis is to investigate the optical transmission and image contrast attainable when imaging tissue using light at near infrared (NIR) and short-wave infrared (SWIR) wavelengths. The motivation for this work is to provide guidance for researchers developing SWIR emitting nanoprobes as contrast agents for the identification of cancerous lesions. The studies described in this thesis were carried out using both tissue simulating phantoms and biological tissues.

1.1 CANCER AND CLINICAL MANAGEMENT

Cancer occurs when a group of cells in the body begin to proliferate uncontrollably and spread into the tissues surrounding them [17]. About 39% of the United States population will be diagnosed with cancer in their lifetime and it is the second leading cause of death, following closely behind heart disease [2]. Normal human cells will grow and divide as the body needs them and old or damaged cells are removed in a process known as apoptosis. Cancer develops when apoptosis no longer occurs, leading to a solid collection of these cells known as a tumor. Tumors can encroach into surrounding tissue impairing the body's ability to function [17]. Cells can break off the original tumor and migrate to other parts of the body in a process known as metastasis [15]. Metastasis results in severe impairment of the body's functions and most cancer related deaths are a result of metastatic disease [17].

Clinically, it is important to (i) diagnose tumors at the earliest possible stage, (ii) remove all malignant cells from the site where a tumor is found, and (iii) determine whether cancerous cells have metastasized. Radiological imaging technologies that are in use to

address these concerns mentioned above include MRI, CT, and PET scans. Magnetic resonance imaging (MRI) uses the application of high power magnetic fields to produce images of tissue anatomy [10]. While MRI can be utilized to detect cancer, to determine cancer stage, and to monitor the effectiveness of treatment, MRI is expensive and has a high rate of false positives (specifically for breast cancer) [3]. Another imaging modality in use is computed tomography or CT scanning [3]. A CT scan is formed from a combination of cross-sectional X-ray images of the body in multiple planes allowing for the generation of a 3D image. A drawback of the procedure is exposure to ionizing radiation while the scans are taken [11]. Positron emission tomography or PET scans are also commonly used to detect cancerous lesions. PET scans use dye infused with radioactive tracers and provide information on blood flow, metabolism, and oxygen usage to identify the presence of a cancerous lesion. Once again, the main drawback to the PET scan is the use of the radioactive tracer [18]. In summary, the noninvasive imaging procedures in use today, while effective, are expensive and expose the patient to radiation.

1.2: OPTICAL IMAGING IN CANCER

Alternative imaging techniques are desirable for clinical usage in cancer screening, surveillance, real-time surgical guidance, cancer staging, and monitoring response to cancer therapies. One optical imaging technique under development is fluorescence imaging. *In vivo* fluorescence imaging uses the interaction of non-hazardous optical radiation with endogenous fluorophores or fluorescent labels to provide real-time wide-field images of tissue structure and/or functional components. *In vivo* fluorescence imaging requires an excitation light source, filters to selectively separate fluorophore emissions

from excitation light, and a camera to generate an image of tissue. When imaging subsurface tissues, excitation light must travel through the overlying tissue to reach the fluorescent target. Emitted fluorescence must then propagate back through the overlying tissue in order to be collected at the camera. Fluorescent emissions can be provided by exogenous contrast agents or by autofluorescence. Autofluorescence occurs when tissue naturally fluoresces upon absorbing excitation light [5]. **Figure 1** shows a depiction of *in vivo* fluorescence imaging.

Exogenous contrast agents can be designed to target and bind to specific cells of interest, for example tumor cells and metastatic cells. A natural avenue of using exogenous agents to identify malignant lesions takes advantage of the enhanced permeability and retention (EPR) effect. Contrast agents coated with PEGylated polymers provide long blood circulation half-lives and, while circulating through the blood, accumulate at high levels in tumors because of leaky tumor vasculature and poor lymphatic drainage. Once trapped in the tumor, illumination of the region at the excitation wavelength can allow for the identification of the malignant mass. Exogenous contrast agents can also be designed to target specific cells by conjugating fluorophores to molecular-specific targeting components such as antibodies or peptides [5].

In vivo fluorescence imaging with fluorophores utilizing the visible spectrum for excitation and emission has been widely explored. However, it was discovered that tissue autofluorescence and photon scattering are high at these wavelengths, and there is also a large amount of photon absorption by blood in tissue. For these reasons, as we attempt to image deeper into tissue, spatial resolution and contrast is compromised [5].

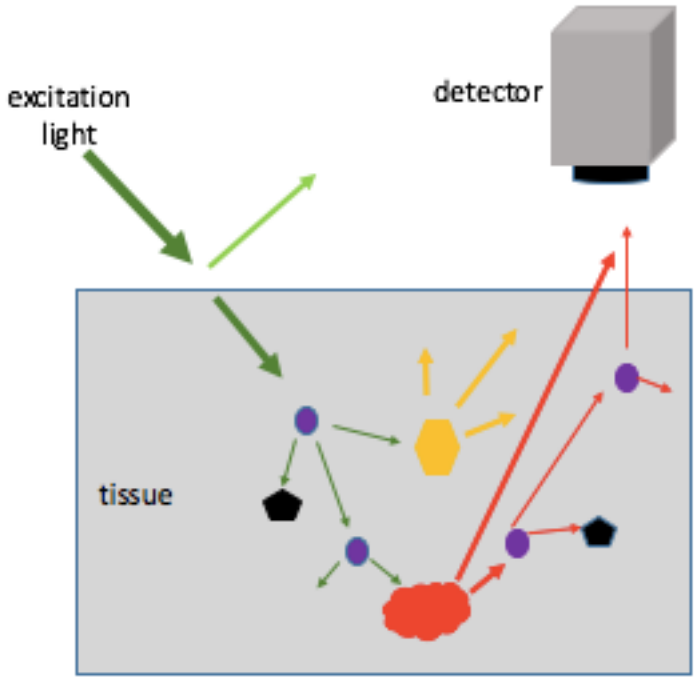

Figure 1: A diagram illustrating light-tissue interactions. An excitation wavelength travels through tissue to the fluorophore causing it to fluoresce and give off an emission signal. These emissions then travel out of the tissue and are picked up by a detector. The dark green arrows represent the excitation light. The lighter green arrow represents the incident light lost due to interface reflection. The purple circles represent scattering interactions. The black pentagons represent absorption events. The red mass stands for the fluorophores identifying the cells of interest and the red arrows represent fluorescent emissions. The gold hexagon displays an autofluorescence event and the gold arrows represent the signal produced by the the autofluorescence event. The narrowing of the arrows in the figure represents signal loss due to scattering.

Figure 1 illustrates the potential interactions between photons and biological tissue. Photons propagating through tissue undergo scattering because of the variation in refractive indices of the biological components in tissue (water, lipid, DNA etc.) [5]. A term used to describe these events is the *scattering coefficient* (μ_s [cm^{-1}]), which is the average number of scattering events per unit path length of photon travel [1]. Another term that is often used to describe scattering is the *reduced scattering coefficient* (μ'_s [cm^{-1}]) which takes the angle of scattering into account as well. Scattering tends to decrease with increasing wavelength in biological tissues, as shown in **Figure 2b**.

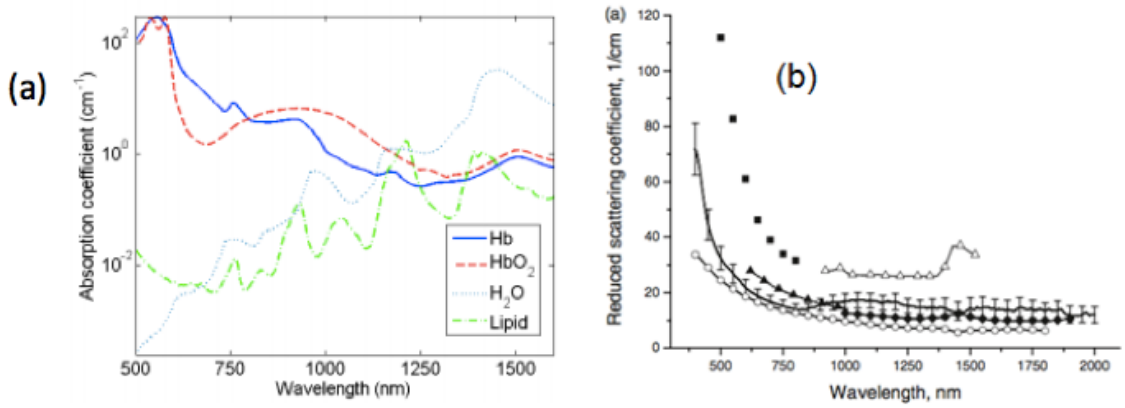

Figure 2: (a) A plot of the absorption spectra of four major tissue components [7]. (b) A plot of the reduced scattering spectra of skin [1].

Tissue is also composed of chromophores such as hemoglobin and water which can absorb photons. Photon absorption is described by the *absorption coefficient*, (μ_a [cm^{-1}]) which is the reciprocal of the average photon path length travelled before absorption [1]. **Figure 2a** shows the absorption spectra of hemoglobin and water. As seen by a comparison of the two spectra, hemoglobin contributes strongly to absorption in the visible spectrum while water contributes to absorption in the SWIR region. An ideal spectral window for imaging purposes should have low photon scattering and absorption [5]. As the scattering coefficient is relatively high in the visible spectrum (400 nm – 700 nm), as seen in **Figure 2b**, a solution has been to use fluorophores with emission spectra in the NIR spectrum (700 nm – 1,000 nm), as the scattering coefficient in this region is smaller. It is believed that the lower scattering coefficient may allow for farther propagation through tissue and to maintain better image contrast.

Using excitation light in the NIR spectrum also greatly reduces autofluorescence. Reduction of autofluorescence is important as it interferes with the detection of fluorophore emissions by adding a signal which can be misconstrued to be fluorophore emissions. A

NIR fluorophore that is currently used clinically for intraoperative imaging is indocyanine green (ICG) with an excitation peak at 807 nm and emission peak at 822 nm. Once introduced into the blood stream, ICG binds tightly to plasma proteins and allows for the structural visualization of anatomical features such as blood vessels, the gastrointestinal tract, and the bile duct [5]. The drawbacks of ICG are the lack of a functional group for molecular specificity and a poor quantum efficiency [22]. A conjugate of ICG, BLZ-100, is under study for use in intraoperative settings. Unlike ICG, BLZ-100 has the ability to bind to and identify specific cells of interest. BLZ-100's peptide component is a 36 amino acid derivative of the CTX peptide found in scorpion venom. It has been proven that the CTX peptide can bind to different types of tumors via molecular interaction with protein components of cholesterol-rich lipid rafts. For this reason, BLZ-100 can identify tumor cells and differentiate them from healthy tissue, greatly aiding a surgeon during tumor removal [4]. Clinical trails using BLZ-100 on melanoma patients undergoing tumor excisions have proven BLZ-100 to be a valuable intraoperative tool for the identification of tumor cells. If tumor cells can be accurately labeled and identified, the number of repeated resection surgeries can potentially be reduced [4]. Another NIR agent under investigation is Cetuximab-IRDye800 for the identification of head and neck tumors. Cetuximab-IRDye800 is a fluorophore labeled with an anti-EGFR antibody. EGFR is targeted as the majority of head and neck tumors overexpress EGFR. The anti-EGFR antibody on the Cetuximab-IRDye800 will bind to the EGFR on the tumor identifying it. A clinical study was performed in which Cetuximab-IRDye800 was administered to patients who were scheduled for surgical resection of carcinoma. NIR fluorescence images were taken both preoperatively and intraoperatively proving Cetuximab-IRDye800 to be

viable for identification of carcinomas both prior to and during surgical resection. **Figure 3** depicts the preoperative and intraoperative results of the clinical studies [12].

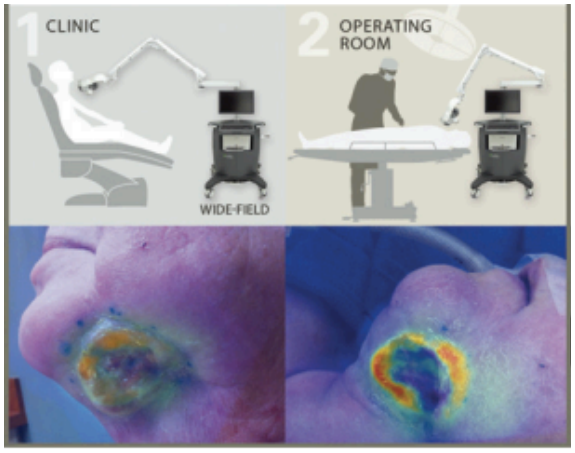

Figure 3: This figure from Rosenthal et al. [12] depicts the stages of the clinical study to test Cetuximab-IRDye800 and the results obtained. As seen from the results, Cetuximab-IRDye800 appears to be a valuable tool for labeling carcinomas both preoperatively and intraoperatively.

1.3: SHORT-WAVE INFRARED IMAGING

As propagation of light is impaired by photon scattering and it is known that scattering decreases with increasing wavelength, there have been investigations into the use of wavelengths beyond the NIR region for imaging purposes. Propagation of light in the SWIR region (~1,000 nm to 2,300 nm), through tissue has been under study as it is believed that these wavelengths may propagate through tissue with lower attenuation than NIR light. Although wavelengths in this region have higher absorption than NIR light, it has been hypothesized that the reduced scattering of the SWIR region could more than compensate for this (see **Figure 2b**) [19].

Sordillo *et. al* conducted a study to examine the propagation of SWIR wavelengths through tissue [13]. Transmission images of *ex vivo* chicken breast tissue were taken with

three black wires of varying thicknesses embedded 1.6 mm deep in the tissue by illuminating with a halogen lamp with wavelengths ranging from 200 nm to 2,500 nm. To test imaging at greater depths, tissue slices were added on top of the sample containing the wires. The contrast of the images of the wires was calculated. It was found that the wavelengths from 650 nm – 900 nm could not penetrate the tissue to provide an image of the wires, while the longer wavelengths from 1,100 nm – 1,870 nm could because of the reduced scattering at longer wavelengths. The 1,100 nm – 1,350 nm wavelength range produced the greatest percent contrast [13] overall.

Another investigation conducted by Zhang *et. al.* examined light penetration of wavelengths of 900 nm – 1,650 nm through tissue. Continuous wave broad band light was passed through a tissue phantom with a grid underneath and images in transmission and reflection geometries were taken. Michelson contrast of the grid imaged through the tissue phantom was used as a metric to evaluate light propagation. A look at the results of both geometries found that a range of 1,300 nm to 1,350 nm offers the highest spatial contrast available at the largest depth and is the best optical range for deep optical imaging [21]. This conclusion is consistent with Sordillo's findings.

Successful usage of SWIR wavelengths for imaging tissue has led some research groups to develop fluorophores with emission spectra in the SWIR region. Some SWIR emitting materials that have been examined for biomedical applications include carbon nanotubes and quantum dots [5,14]. Carbon nanotubes have the ability to emit wavelengths from 800 nm – 1,600 nm, making them desirable for use in *in vivo* hyperspectral imaging. However, the nanotubes have very inefficient photoluminescence because of structural defects arising during synthesis, making them undesirable for clinical usage [14]. SWIR

emitting In-As based core-shell and core-shell-shell quantum dots have also been studied for use in biological applications. These quantum dots provide a much higher quantum yield than carbon nanotubes. However, they are known to be unstable in aqueous media and almost all quantum dots degrade upon coming into contact with air or water. In order to be used in a biomedical application, they must be placed inside an inorganic shell or have an oxide coating applied [14].

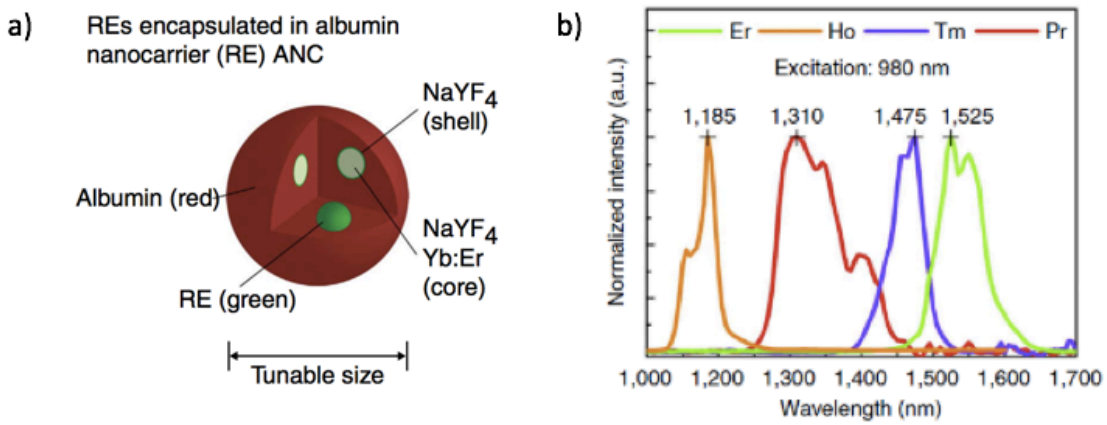

Figure 4: (a) Diagram of rare-earth doped nanoparticles encapsulated in an albumin shell to allow for biocompatibility [8]. (b) Emission spectra of different rare-earth doped nanoparticles [7].

Recently, rare-earth (RE) doped nanomaterials have been considered as candidate SWIR emitting fluorophores for *in vivo* use [8]. RE doped nanocomposites are potentially advantageous over other emitters as they require low power for excitation and have bright emissions at specific SWIR wavelengths [8]. Individual RE nanoparticles can be encapsulated into an albumin carrier to make them biocompatible and allow functionalization with targeting molecules (**Figure 4a**). RE's are composed of a $NaYF_4$ core which is doped with ytterbium (Yb) and one of the following rare-earth elements: erbium (Er), holmium (Ho), thulium (Tm), or praseodymium (Pr). The choice of rare-earth

element will determine which wavelengths the particle emits as shown by the emission spectra in **Figure 4b**. The nanoparticles under study in this thesis are doped with erbium and therefore emit wavelengths centered around 1,550 nm upon excitation by a 980 nm source. Detection of this fluorescence is dependent upon the properties of the tissue and biological components surrounding it. Water, melanin, hemoglobin, and lipids will absorb the emitted wavelengths while the physical morphology and composition of the tissue itself will lead to scattering of the wavelengths [20]. The question that remains to be answered is do the SWIR emissions from these nanoparticles propagate farther through tissue and allow for better tissue resolution than NIR emissions?

1.4: SCIENTIFIC RATIONALE FOR THIS WORK

1.4.1: Theory

While there have been studies investigating the behavior of NIR and SWIR wavelengths through tissue, there have been very few studies conducted that directly compare the propagation of NIR and SWIR wavelengths through tissue. A direct comparison of the propagation of light from these two wavelength regions in tissue would help support the development of optical contrast agents and identify their suitable clinical applications.

	Wavelength (nm)	Reduced Scattering Coefficient (1/mm)	Absorption Coefficient (1/mm)	Transport Mean Free Path (mm)
Skin	780	1.71	0.0873	0.56
	980	1.23	0.0757	0.76
	1550	1	0.8	0.55

Table 1: Reduced scattering and absorption coefficients for skin in the NIR (780 nm and 980 nm) and SWIR (1,550 nm) regions. The coefficients for 780 nm and 980 nm are from the Virtual Photonics website (www.virtualphotonics.org), while the coefficients for 1,550 nm are from Troy *et. al.* [16]. Transport mean free path was calculated using the formula $1/(\mu_a + \mu'_s)$.

Propagation of photons in tissue is characterized by tissue absorption and scattering coefficients, explained in Section 1.2. The accumulation of multiple scattering events will lead to randomization of the direction of photon propagation [9] compromising image contrast and resolution. **Table 1** displays the absorption and scattering coefficients of skin at selected NIR and SWIR wavelengths. The coefficients for 780 nm and 980 nm are from the Virtual Photonics website (www.virtualphotonics.org), while the coefficients for 1,550 nm are from Troy *et. al.* [16] As seen in **Table 1,** the SWIR region (1,550 nm) has the lowest scattering coefficient and therefore should provide the highest image resolution.

The transport mean free path, calculated as $1/(\mu_a + \mu'_s)$, describes the distance it takes for light to become diffuse. Ballistic photons follow their original trajectory and propagate in the forward direction, however diffuse photons travel in directions uncorrelated with their original trajectory, resulting in a reduction of depth penetration of the incident light. A higher transport mean free path means a higher penetration distance and therefore a higher transmission [9]. From the transport mean free paths calculated in **Table 1**, it appears as if the 980 nm wavelength in the near infrared region will have the highest transmission.

1.4.2: Overview of Experiments

The work described in this thesis attempts to compare the propagation of NIR and SWIR wavelengths through tissue. The goal is to determine whether SWIR wavelengths are the best option for use in fluorescent imaging probes. Light at 780 nm was tested to represent the NIR spectrum. The 1,550 nm wavelength was used for testing as it approximates the SWIR wavelength that erbium-doped rare-earth nanoparticles fluoresce

at. 980 nm was also tested as it is the wavelength that is used to excite the rare-earth nanoparticles; it was important to also ensure that the excitation wavelength has the ability to travel through tissue and reach the nanoparticles. The ability of the wavelengths to transmit through tissue and their ability to resolve surrounding tissues was examined through transmission and contrast experiments explained thoroughly in Chapter 2. Silicone phantoms were tested first (see Section 3.1 for more information) as they provide a simulation of the optical properties of tissue while being easy to make, durable, nonperishable, and easy to handle. Water based phantoms with Intralipid were tested next in order to introduce a tissue simulating phantom with water content (see Section 3.2 for more information). Next, *ex vivo* chicken breast and chicken liver tissue were tested to obtain information about the transmittance and resolving ability of the wavelengths of interest in real biological tissue. Finally, a pilot study was conducted to examine the dual emission properties of the rare earth nanoprobes.

1.5: HYPOTHESES

From section 1.4.1, it appears that the 980 nm wavelength should have the highest transmission. Although there is a decline in reduced scattering coefficient from the NIR region to the SWIR region, it appears to be small in comparison to the increase in absorption coefficient in the SWIR region. For this reason, NIR wavelengths should propagate through tissue with less attenuation and provide better transmission than the SWIR spectral region. The reduction in reduced scattering coefficient from the NIR region to the SWIR region however, should provide better tissue resolution, provided enough photons can be detected.

1.6: REFERENCES

1. Bashkatov, A., *et al*. “Optical Properties of Human Skin, Subcutaneous and Mucous Tissues in the Wavelength Range from 400 to 2000 nm.” *Journal of Physics D: Applied Physics*, vol. 38, no. 15, 2005, p. 2543–2555.
2. “Cancer Statistics.” *Cancer Statistics,* National Cancer Institute, www.cancer.gov/about-cancer/understanding/statictics.
3. Fass, L. “Imaging and Cancer: A Review.” *Molecular Oncology*, vol. 2, no. 2, 2008, p. 115–152.
4. Franklin H., *et al*. “Clinical Development of BLZ-100 For Real-Time Optical Imaging of Tumors During Resection”, in Proc. SPIE 9696, *Molecular-Guided Surgery: Molecules, Devices, and Applications II*, p. 96960V-1, 2016.
5. Hong, G., *et al*. “Near-Infrared Fluorophores for Biomedical Imaging.” *Nature Biomedical Engineering*, vol. 1, no. 1, 2017, p. 0010.
6. Krans, B. “PET Scan” *Healthline*, Healthline Media, 2 Nov. 2015, www.healthline.com/health/pet-scan#uses2.
7. Nachabé R., *el al.* “Estimation of Biological Chromophores Using Diffuse Optical Spectroscopy: Benefit of Extending the UV-VIS Wavelength Range to Include 1000 to 1600 nm.” *Biomedical Optics Express*, vol. 1, no. 5, 2010, p. 1432-1442.
8. Naczynski, D., *et. al*. "Rare-Earth-Doped Biological Composites as *In Vivo* Shortwave Infrared Reporters." *Nature Communications*, vol. 4, 2013, p. 2199.
9. Ntziachristos, V. “Going Deeper than Microscopy: the Optical Imaging Frontier in Biology.” *Nature Methods*, vol. 7, no. 8, 2010, p. 603–614.
10. Radiological Society of North America (RSNA) and American College of Radiology (ACR). “Magnetic Resonance Imaging (MRI) - Body.” *Body MRI - Magnetic Resonance Imaging of the Chest, Abdomen and Pelvis*, www.radiologyinfo.org/en/info.cfm?pg=bodymr.
11. Radiological Society of North America (RSNA) and American College of Radiology (ACR). “Computed Tomography (CT) - Body.” *Body CT (CAT Scan)*, www.radiologyinfo.org/en/info.cfm?pg=bodyct.
12. Rosenthal, E., *et al*. “Safety and Tumor Specificity of Cetuximab-IRDye800 for Surgical Navigation in Head and Neck Cancer.” *Clinical Cancer Research*, vol. 21, no. 16, 2015, p. 3658–3666.
13. Sordillo, L., *et al*. “Deep Optical Imaging of Tissue Using the Second and Third near-Infrared Spectral Windows.” *Journal of Biomedical Optics*, vol. 19, no. 5, 2014.
14. Thimsen, E., *et al*. “Shortwave-Infrared (SWIR) Emitters for Biological Imaging: a Review of Challenges and Opportunities.” *Nanophotonics,* vol. 6, no. 5, 2017, p. 1043-1054.

15. Tichauer, K., *et al*. "Microscopic Lymph Node Tumor Burden Quantified by Macroscopic Dual-Tracer Molecular Imaging." *Nature Medicine*, vol. 20, no. 11, 2014, p. 1348-1353.

16. Troy, T., *et al.* "Optical Properties of Human Skin in the Near Infrared Wavelength Range of 1000 to 2200 nm." *Journal of Biomedical Optics*, vol. 6, no. 2, 2001, p. 167-176.

17. "What is Cancer?" *National Cancer Institute*, 9 Feb. 2015, www.cancer.gov/aboutcancer/understanding/what-is-cancer.

18. "What Wavelength Goes With a Color?" *NASA*. NASA, n.d. Web. 21 Dec. 2016.

19. Wilson, R., *et al*. "Review of Short-Wave Infrared Spectroscopy and Imaging Methods for Biological Tissue Characterization." *Journal of Biomedical Optics*, vol. 20, no. 3, 2015, p. 030901.

20. Zevon, M., *et al.* "CXCR-4 Targeted, Short Wave Infrared (SWIR) Emitting Nanoprobes for Enhanced Deep Tissue Imaging and Micrometastatic Cancer Lesion Detection." *Small*, vol. 11, no. 47, 2015, p. 6347-57.

21. Zhang, H., *et al.* "Penetration Depth in Tissue-Mimicking Phantoms From Hyperspectral Imaging in SWIR in Transmission and Reflection Geometry." in Proc. SPIE Vol. 9703, *Optical Biopsy XIV: Toward Real-Time Spectroscopic Imaging and Diagnosis*, p. 970311, 2016.

22. Zhu B., *et al*. "A Review of Performance of Near-Infrared Fluorescence Imaging Devices Used in Clinical Studies." *The British Journal of Radiology*, vol. 88, no. 1045, 2015.

CHAPTER 2: EXPERIMENTAL METHODS

2.1: INSTRUMENT SETUP

To examine the propagation of the NIR and SWIR wavelengths through tissue simulating phantoms and *ex vivo* tissues, the instrument setup depicted in **Figure 5** was implemented to capture transmission and contrast images.

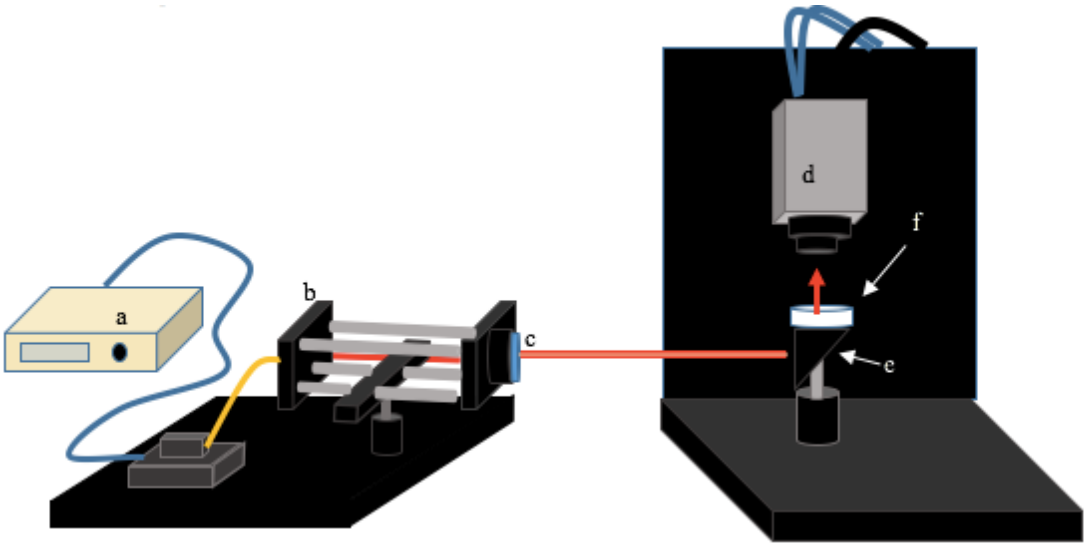

Figure 5: The instrument set-up for transmission and contrast imaging at NIR and SWIR wavelengths. Light from single-mode fiber-coupled lasers at 780 nm, 980 nm, and 1550 nm was transmitted through a collimating lens and directed onto a silver-coated mirror. The mirror deflected the beam vertically toward the imaging camera. Each sample was centered on the collimated beam. (a) Power supply, (b) fiber-coupled beam output, (c) collimating lens, (d) camera, (e) silver-coated mirror, (f) tissue phantom or *ex vivo* sample

u

Light from each of three single-mode fiber-coupled lasers was incident upon tissue-simulating phantoms or tissue samples. 780 nm was used to represent the NIR spectral region, while 980 nm was tested as the rare-earth doped nanocomposites being studied are excited by this wavelength. 1,550 nm light was evaluated as this is the wavelength region in which the erbium-doped rare-earth nanoparticles exhibit luminescent emissions.

Each laser beam was collimated to a 27 mm diameter ($1/e^2$) with the use of a 150 mm focal length, 2" diameter achromatic doublet lens (Thorlabs, AC508-150-C-ML). This

beam was then incident on a silver-coated mirror (Thorlabs, PFE10-P01) mounted at a 45° angle, which deflected the beam so that it was incident on the center of each tissue phantom or tissue sample. A camera was mounted above the sample to acquire transmission images. To obtain contrast data, the same instrumental set-up was used, however a reflective Ronchi grating with 0.5 cycles/mm was placed directly below the tissue sample.

Two different cameras, one with a silicon sensor and one with an InGaAs sensor, were utilized to measure the transmitted light intensity and image contrast. The silicon camera (Andor, Zyla 5.5 sCMOS) acquires images that are 2,556 pixels by 2,158 pixels in size. The InGaAs camera (Sensors Unlimited, GA1280JS) takes images that are 1,280 pixels by 1,024 pixels. Both cameras were set to acquire 12-bit image data. The 780 nm images were taken by the silicon camera as it is sensitive to visible and NIR wavelengths, covering about 400 nm to 800 nm. The 980 nm and 1550 nm images were taken with an InGaAs camera that is sensitive to light in the SWIR region (900 – 1,700 nm). The reason for the use of two different cameras is evident in **Figure 6.** The silicon camera has a very low quantum efficiency in the SWIR region while the InGaAs camera has a very low quantum efficiency at the visible and the NIR wavelength region. Use of only one camera for all wavelengths, as seen in previous studies, could lead to an unfair comparison of images. Using cameras that are optimized for the specific wavelength regions of interest allowed for the elimination of this potential source of error.

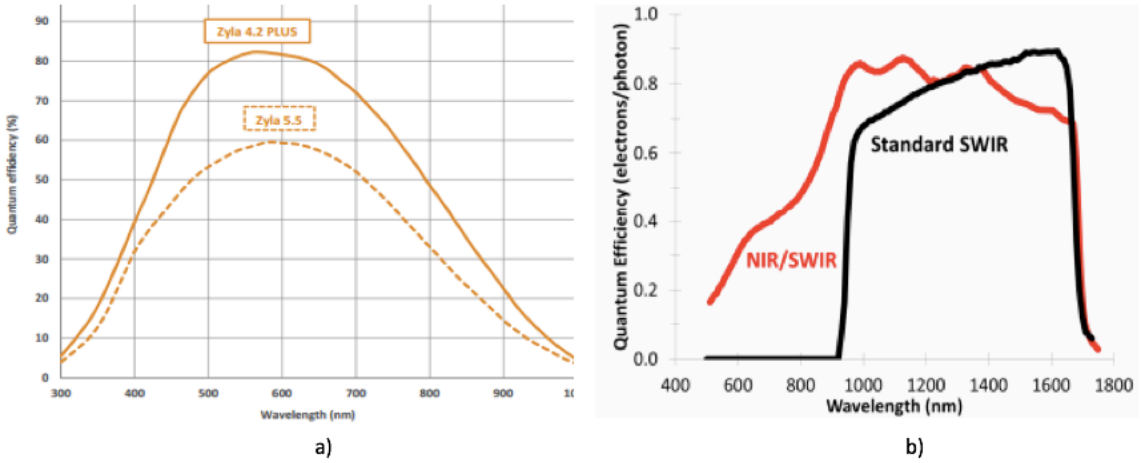

Figure 6: (a) Quantum efficiency curve of the Andor, Zyla 5.5 sCMOS camera. (b) Quantum efficiency curve of the Sensors Unlimited, GA1280JS camera. (The "Standard SWIR" model was used here).

2.2: CALCULATION OF TRANSMISSION AND CONTRAST

2.2.1: Calculation of Transmission

To quantify the transmission of each sample, the wavelength (780 nm, 980 nm, or 1,550 nm) which exhibited the highest apparent transmission was used to determine a laser power level and camera exposure time to be used for the entire data set. The power level and exposure time were adjusted to bring the image of the thinnest sample to just below saturation, ensuring that images would not be saturated for the remaining samples or wavelengths. Power levels and exposure times were then kept constant. All camera auto-correction features such as offset, gain, dark-level adjust etc. were turned off. To calculate transmission, a rectangular region of interest encompassing the incident beam was selected using each camera's software package. The software calculated the mean pixel value within the region of interest. The higher the mean pixel intensity value the greater the transmission of the beam.

2.2.2: Calculation of Image Contrast

Contrast refers to our ability to discern different intensity levels within an image. After the Ronchi grating images were collected, they were processed with a MATLAB algorithm to calculate contrast as illustrated in **Figure 7**. The user defines the region of the image in which to calculate the contrast and the mean pixel intensities of each column in this region are calculated. The algorithm then calculates the difference between each pair of maxima and minima and determines which has the greatest difference. The minima and maxima that produced the greatest difference are then used in the Michelson contrast equation (1) to calculate the maximum contrast of the image:

$$Contrast\ (\%) = \frac{(Maximum\ Pixel\ Intensity - Minimum\ Pixel\ Intensity)}{(Maximum\ Pixel\ Intensity + Minimum\ Pixel\ Intensity)}\ X\ 100 \quad (1)$$

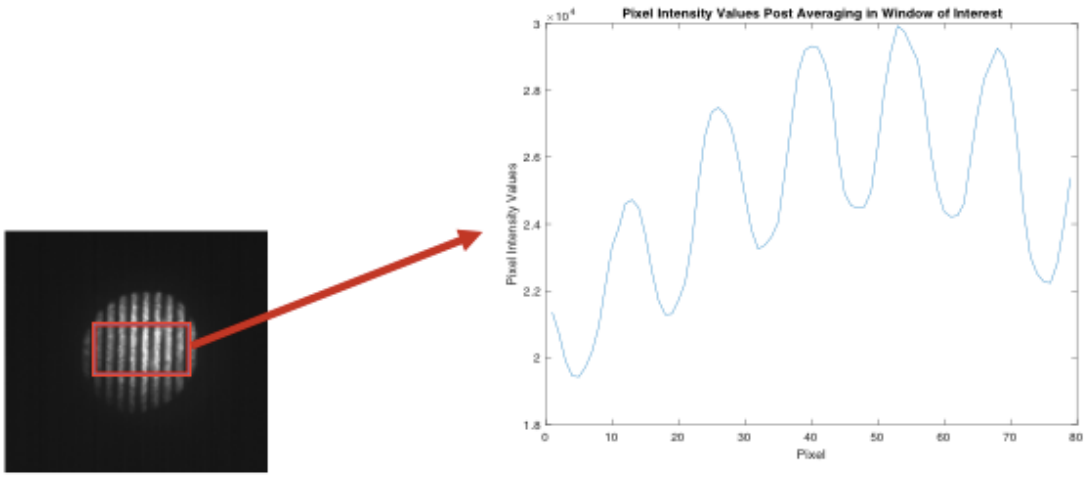

Figure 7: A diagram illustrating the algorithm used to calculate contrast. The user defines the region of interest of the image (indicated by the red box). The mean pixel intensity for each column in the region is calculated and the minima and maxima identified (as displayed by the plot in the diagram). The mean is calculated as it provides a more accurate representation of the mean pixel intensities than a point measurement would allow. The algorithm then calculates the difference between each pair of maxima and minima and determines which pair has the greatest difference. The minima and maxima that produced the greatest difference are then used in the Michelson contrast equation (1) to estimate the maximum image contrast.

2.3: CORRECTING FOR CAMERA EXPOSURE TIMES

As explained in Section 2.2.1, in order to obtain the transmission data sets, a beam of 780 nm, 980 nm or 1550 nm light was transmitted through each tissue phantom or sample. The wavelength that had the highest apparent transmission was then used to set the laser power level and camera exposure time for that data set. While the silicon camera allowed for the manual setting of any arbitrary exposure time, the InGaAs camera has eleven preset exposure time settings, called "OPR" settings. Due to the differences in attenuation of light at the wavelengths tested, the laser power level and camera exposure time that gave a good image for one wavelength sometimes resulted in dark or saturated images at the other wavelengths, which could not be used for quantitative comparison between samples. For this reason, images were acquired at different exposure time settings, and then post-processed to convert pixel values to equivalent exposure times. For example, if one image generated a mean pixel value of 1000 with an exposure time of 10 ms, and a second image generated a mean pixel value of 1000 at an exposure time of 5 ms, then the second image could be corrected to an equivalent mean pixel value of 2000 for a 10 ms exposure time. In practice, this conversion must consider the effect of dark current and other noise sources, so this was examined experimentally.

To determine the conversion factor from one OPR setting to the next, an experiment was conducted where the 1550 nm beam was transmitted through one of the silicone phantoms (see Section 3.1 for more details on silicone phantoms) and the laser power level adjusted so the image generated at the OPR setting with the longest exposure time (2.36 ms) contained pixels that were just below saturation. While keeping this laser power level constant, additional images were taken at 0.163 ms, 0.397 ms, 0.968 ms, 2.36 ms (OPR

settings 2-5). All auto-adjust settings for the camera were switched off. The mean pixel intensities were measured within a selected region of interest in each image and plotted against the known exposure time. If the y-intercept of this plot was zero or close to zero, multiplying the recorded mean pixel intensity by the ratio between the original exposure time and the desired exposure time should accurately correct the recorded pixel intensity. As displayed in **Figure 8a**, the first experiment displayed a y-intercept of about 400 pixel values (on a 12-bit scale, 0-4095). The experiment was repeated with the lens cap on and the mean pixel intensity measured, to determine the background level at each exposure time. These background values were subtracted from each phantom measurement and these "background-corrected" mean pixel intensities plotted against exposure time. From **Figure 8b,** it is evident that once the background level is removed, it is possible to correct for measurements acquired at different exposure times.

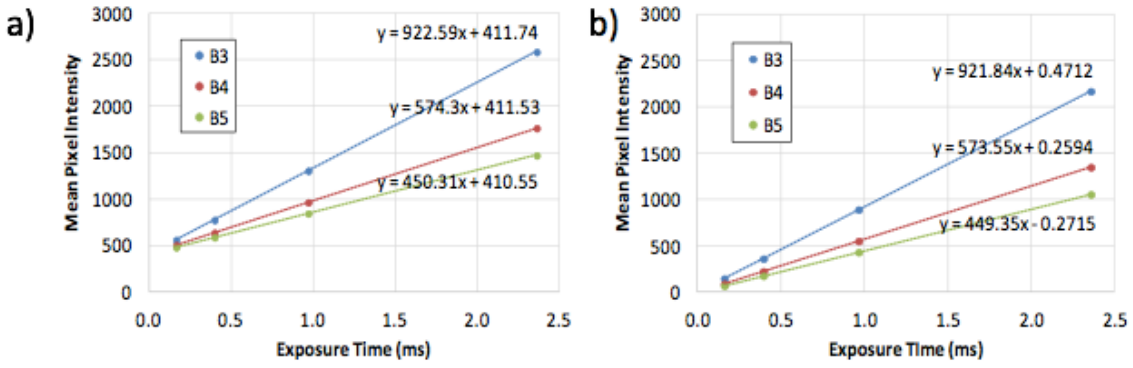

Figure 8: (a) Raw mean pixel intensities measured as a function of camera exposure time for three different silicone phantoms (B1, B2, B3). The y-intercept is significantly greater than zero, indicating there is a background level that has not been accounted for. (b) After measuring and removing the background pixel value at each exposure time, the y-intercept is almost zero, indicating that after background correction, using ratios of exposure times to correct for measurements acquired at different exposure time is feasible.

CHAPTER 3: EXPERIMENTS USING TISSUE SIMULATING PHANTOMS

3.1: SILICONE PHANTOMS

3.1.1: Fabrication and Characterization of Silicone Phantoms

Experiments were conducted on tissue-simulating phantoms in an attempt to test the hypothesis that NIR wavelengths have greater propagation through tissue than SWIR wavelengths. A second hypothesis tested was that SWIR wavelengths will allow for imaging with increased contrast than shorter wavelengths. Solid phantoms using silicone as a host matrix were initially chosen as they are non-perishable and durable. These phantoms were fabricated with addition of titanium oxide (TiO) as a scattering agent, and nigrosin dye as an absorbing agent. Two sets of phantoms were made and tested. One set, shown in **Figure 9b,** had constant thickness but varying amounts of TiO in order to create phantoms with varying scattering properties. Phantoms in the other set, shown in **Figure 9c**, contained the same amount of TiO but had varying thicknesses.

Phantoms in the first set were each 60 mm in diameter and had a fixed thickness of 9.2 mm. 0.25 mL of nigrosin from a 1.5 g/L stock solution was added to each of the phantoms in this set, keeping the absorption constant. Each phantom in this set contained a different amount of TiO (0.03g, 0.04g, 0.06g, 0.08g, or 0.09g). The optical properties of each phantom (absorption coefficient, μ_a (mm^{-1}), and reduced scattering coefficient, μ'_s (mm^{-1})) were directly measured by spatial frequency domain imaging (SFDI) at nine different wavelengths ranging between 396 nm to 851 nm, using a commercial system made available by collaborators at Boston University. The optical properties of each phantom were estimated at the wavelengths of interest for this study (780 nm, 980 nm, and 1550 nm) by applying a MATLAB algorithm to the SDFI data. The algorithm uses the

MATLAB function "power" to solve for the roots that best fit a curve to the data. Interpolation was then performed to determine the scattering coefficient at 780 nm while extrapolation provided an estimate of the scattering coefficient at 980 nm and 1550 nm. The measured scattering coefficients of each phantom at the wavelengths used by the SFDI system are depicted as filled circles in **Figure 9a**, while estimated values are shown as open circles.

a)

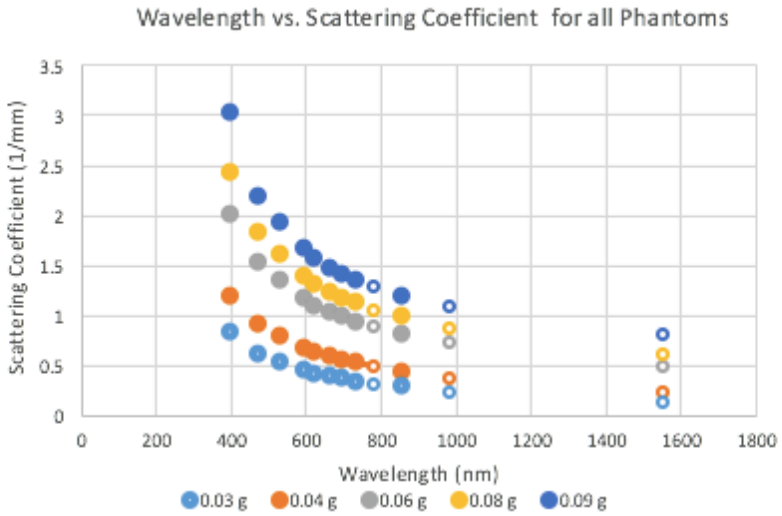

b)

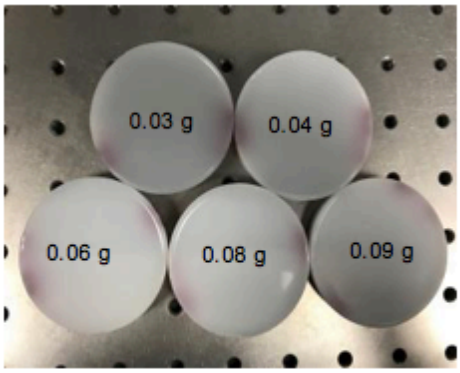

c)

Figure 9: (a) Plot of the reduced scattering coefficients (μ_s') calculated from SFDI at nine wavelengths between 351 nm and 851 nm (closed circles). Estimated values for μ_s' at 780 nm, 980 nm, and 1550 nm are shown as open circles. (b) An image of the phantom set with varying amounts of TiO. (c) An image of the phantom set with varying thickness.

The second set of phantoms was made with constant absorption and scattering coefficients (all contained 0.25 mL of nigrosin and 0.06 g TiO), but varying thickness (5.9 mm, 6.5 mm, 7.9 mm, 9.4 mm, and 11.0 mm), **Figure 9c**. As these phantoms were prepared with the same amounts of nigrosin and TiO as the phantom with 0.06 g TiO measured by SFDI above, they were assumed to have the same optical properties and an independent measurement using SFDI was not conducted.

3.1.2: Experiments with Silicone Phantoms - Methods

As explained in Chapter 2, transmission and contrast experiments were performed on all tissue simulating phantoms and tissue samples. For transmission experiments using the silicone phantom set with varying scattering coefficients, light at 1,550 nm was incident on the phantom with the lowest scattering coefficient. The laser power and camera exposure time were adjusted such that the mean pixel intensity measured within a region of interest encompassing the beam was just below saturation. This ensured that measurements on the other phantoms in the set (with higher scattering) would not generate saturated images. A laser power of 5.43 mW and a camera exposure time of 0.163 ms were used for all measurements at 1,550 nm. Measurements at 980 nm were taken with the same laser power but with a longer camera exposure time of 2.36 ms, with the measured mean pixel intensity then corrected, as explained in Chapter 2, to obtain the mean pixel intensity that could have been expected at an exposure time of 0.163 ms. The exposure time was increased for the 980 nm wavelength to allow for a better qualitative comparison of the transmission results. The same procedure was repeated for the silicone phantom set of varying thicknesses. The thinnest phantom of the set (5.9 mm) was used to determine a

power of 4.69 mW and an exposure time of 0.163 ms at 1550 nm. The 980 nm images were also taken with an exposure time of 2.36 ms to provide a qualitative comparison of images. Quantitative values were corrected to the generate the values that would have been recorded at 0.163 ms.

One additional correction was made to the mean pixel intensities recorded at 980 nm. The InGaAs camera (Sensors Unlimited, GA1280JS) which was used to take the images at 980 nm and 1550 nm has a lower quantum efficiency at 980 nm than 1,550 nm (**Figure 6b**). At 980 nm, the quantum efficiency is about 65%, while at 1,550 nm the value is 90%. Due to the difference in quantum efficiency, the camera will produce a pixel value at 980 nm compared to 1,550 nm, under the same incident light intensity. To correct for this, mean pixel intensities taken at 980 nm were multiplied by the ratio of the quantum efficiency at 1,550 nm (90%) to the quantum efficiency at 980 nm (65%), a factor of about 1.38.

For the contrast experiments with each phantom set, the incident laser power and camera exposure times were adjusted individually for each phantom at each wavelength to yield the highest contrast. The goal of the contrast experiments was purely to see which wavelength could provide the highest contrast imaging through tissue, independent of signal level.

3.1.3: Experiments with Silicone Phantoms – Results

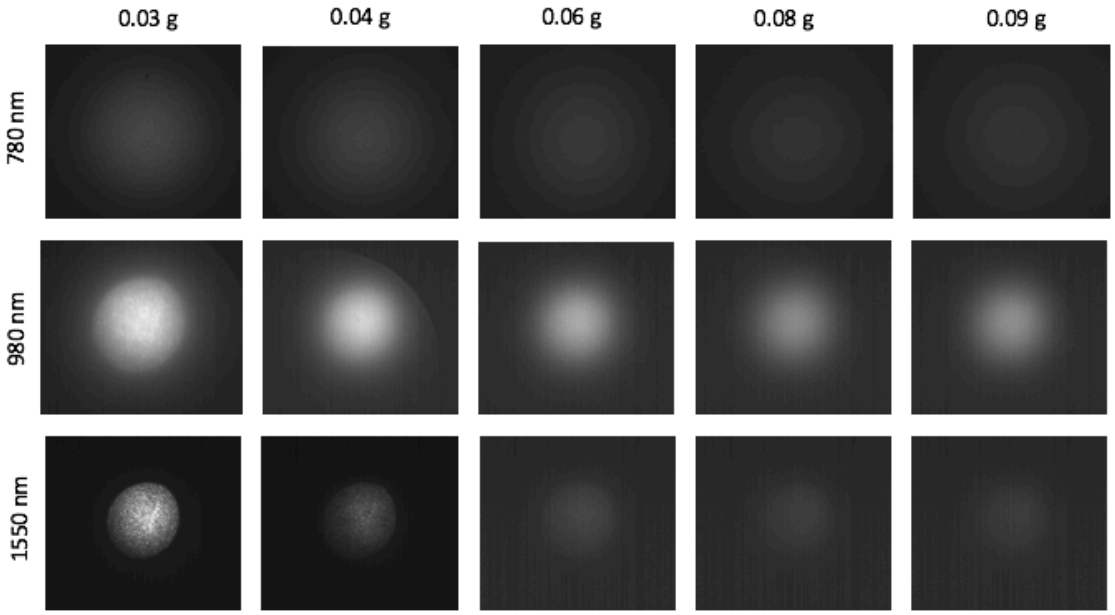

Figure 10: Transmission images for the phantom set containing varying amounts of the scattering agent TiO. All images were taken at an incident laser power of 5.43 mW. The 780 nm and 1550 nm images were taken at an exposure time of 0.163 ms, while the 980 images were taken at an exposure time of 2.36 ms.

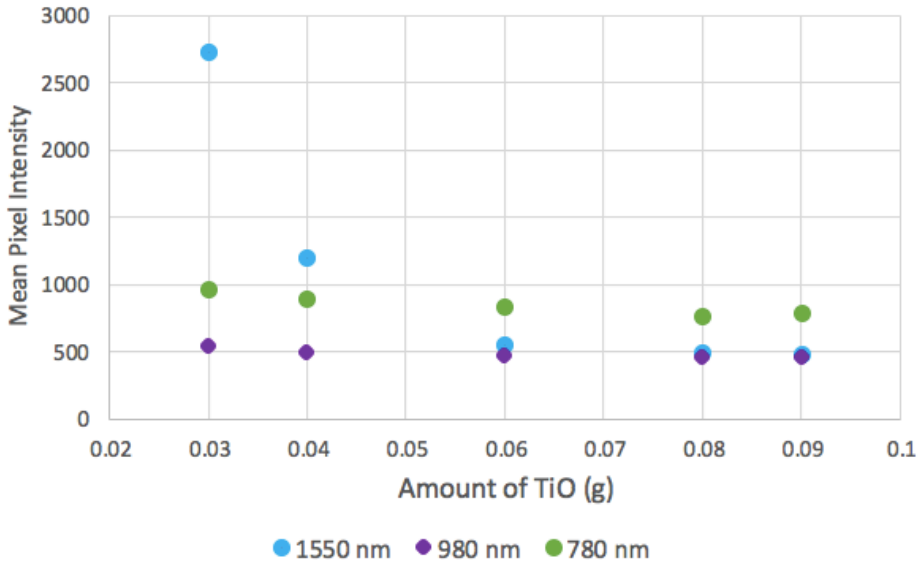

Figure 11: Mean pixel values from transmission images at 780 nm, 980 nm, and 1550 nm shown in **Fig. 10**. The values shown at 980 nm were corrected for exposure time. As the amount of TiO in the phantom increases, the transmission decreases across all wavelengths.

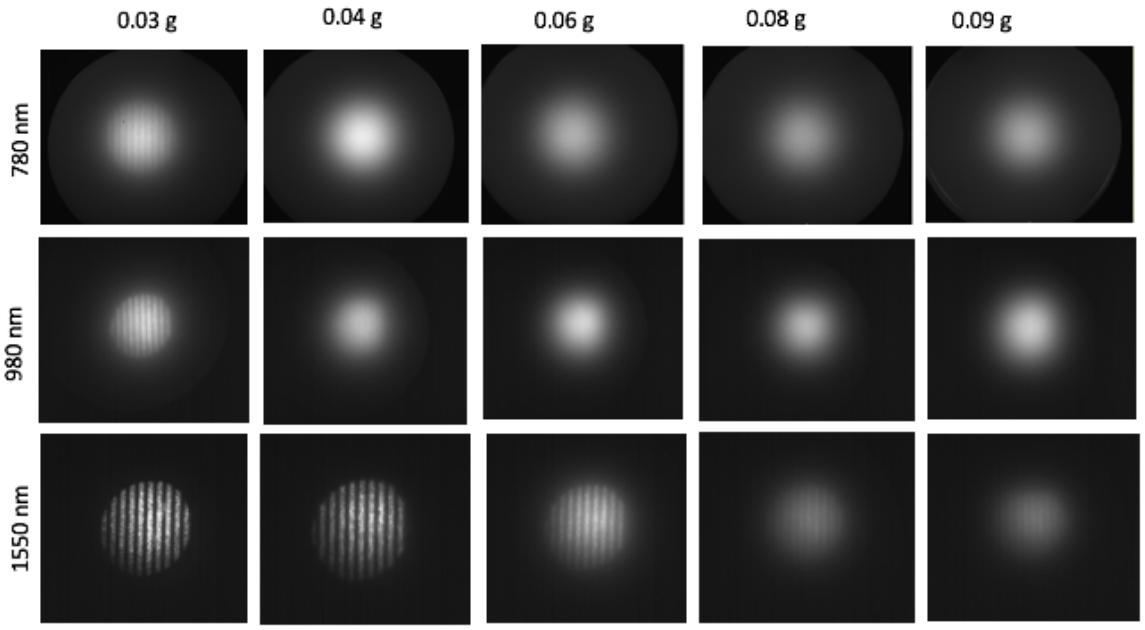

Figure 12: Transmission images obtained from the contrast experiments of the phantom set with varying amounts of TiO. As the amount of TiO increased, the contrast that could be obtained decreased. The 1,550 nm wavelength appears to provide images with the best contrast at all scattering levels.

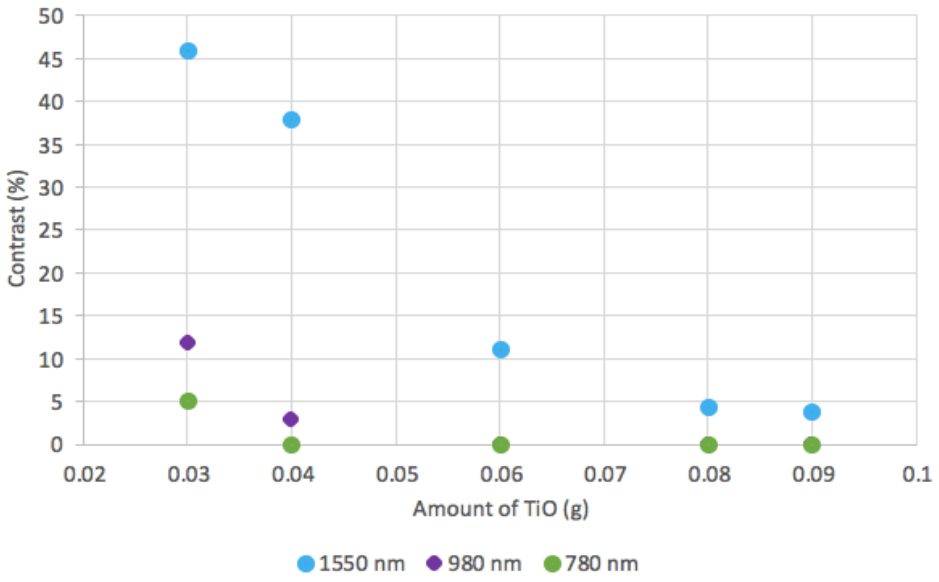

Figure 13: Plot of the maximum image contrast obtained for each scattering phantom at 780 nm, 980 nm, and 1550 nm. 1550 nm provides images with the best contrast.

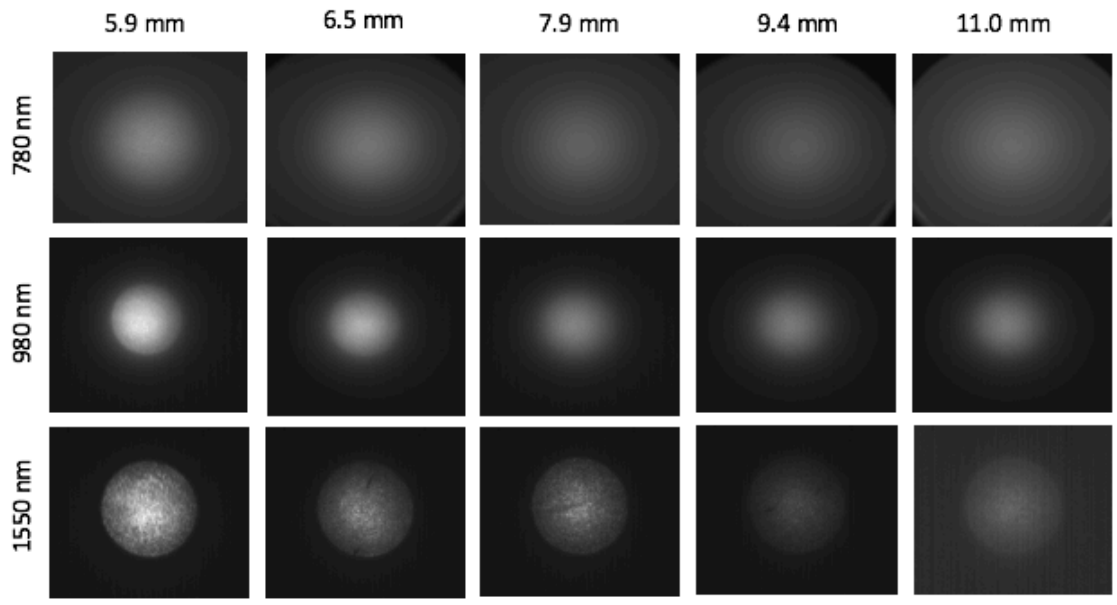

Figure 14: Transmission images obtained from experiments with phantoms of varying thicknesses. As phantom thickness increases, the amount of transmitted light decreases for all wavelengths. All images were taken with an incident laser power of 4.69 mW. However, the 780 nm and 1550 nm images were taken at an exposure time of 0.163 ms, while the 980 nm images were taken at an exposure time of 2.36 ms.

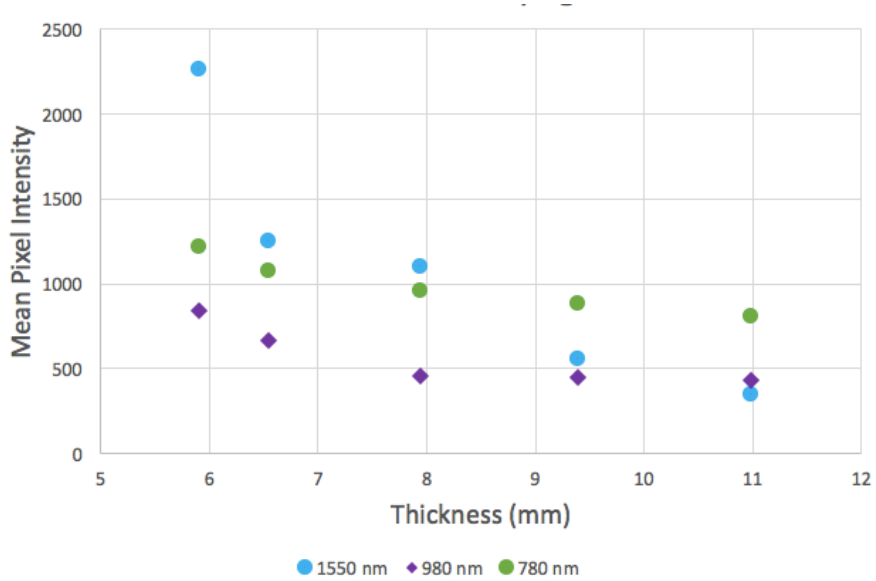

Figure 15: Mean pixel values calculated from transmission images at 780 nm, 980 nm, and 1,550 nm wavelengths through the phantom set with varying thicknesses. The mean pixel values reported at 980 nm were corrected for camera exposure time and quantum efficiency. As phantom thickness increases, the transmission decreases across all wavelengths.

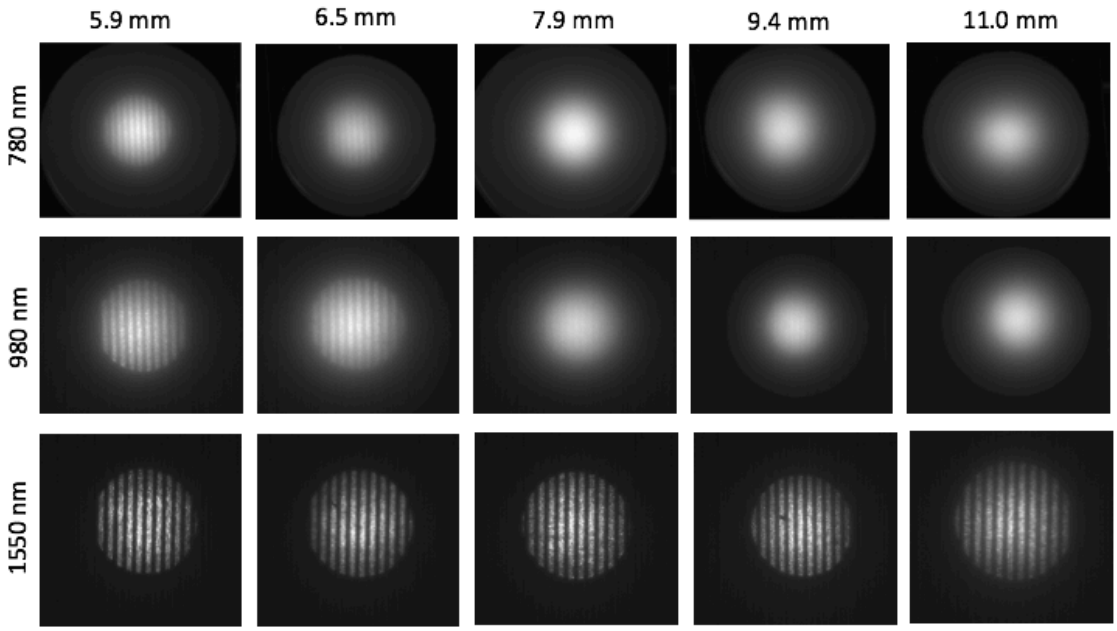

Figure 16: Images obtained from experiments to assess image contrast through the phantom set of varying thickness. As phantom thickness increased, image contrast decreased for all wavelengths. Imaging at 1,550 nm appears to provide images with the highest contrast.

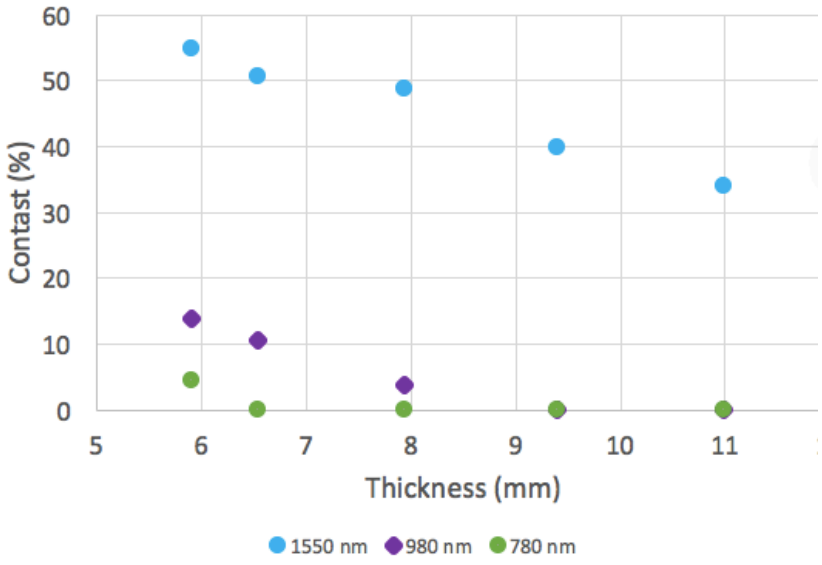

Figure 17: Maximum image contrast measured through phantoms of varying thickness at 780 nm, 980 nm, and 1,550 nm. 1,550 nm provides images with the highest contrast, for all phantom thicknesses tested.

3.2: WATER/INTRALIPID PHANTOMS

3.2.1: Justification of Utilizing Water/Intralipid Phantoms

While silicone phantoms have excellent long-term stability, they lack the absorbing characteristics of water (see **Figure 18**), which is a major contributor to absorption in tissue at SWIR wavelengths. In order to more accurately simulate the absorption characteristics of tissue, a water-based phantom was required which accurately mimicked human tissue at each of the wavelengths being studied.

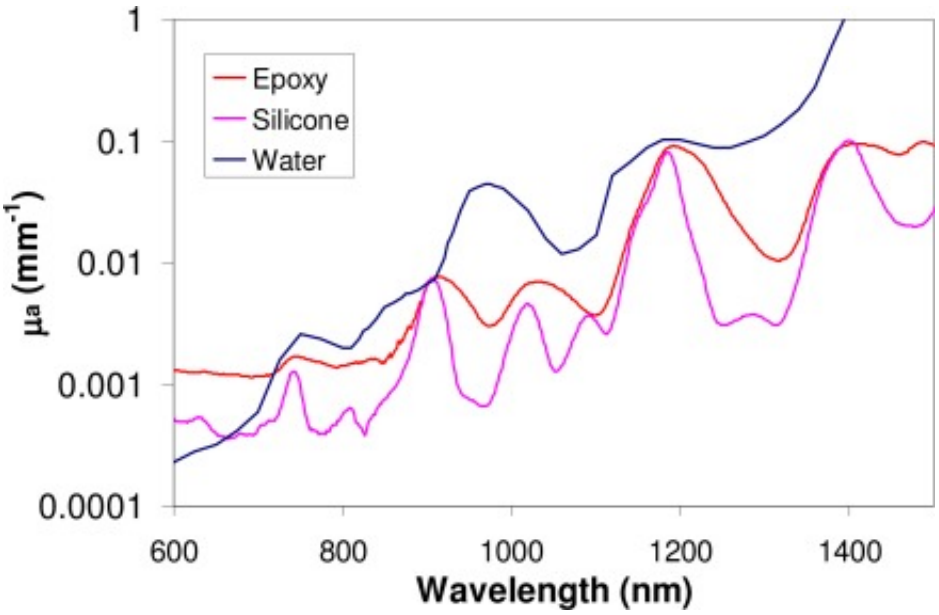

Figure 18: Plot of the absorption coefficient of epoxy, silicone, and water at wavelengths in the visible, NIR, and SWIR regions [1]. The absorption coefficient of silicone is lower than that of water at 780 nm and 980 nm, and probably also than at 1550 nm.

A literature search suggested a variety of phantom recipes. For a solid tissue-simulating phantom, Cubbedu *et al.* suggested using a matrix of 1% agar to provide a phantom that is easy to handle while having a negligible effect on the scattering and absorption coefficients of the phantom [4]. While the addition of water to agar simulates the absorbing properties of tissue, it has not been proven that agar itself does not contribute to

absorption across the wavelengths of interest in this study. Also it was necessary to include a component to accurately mimic the scattering properties of tissue, which this recipe did not include. For these reasons, another solution was desired. Intralipid, an emulsion of soybean oil and water, has been widely used as a scattering agent in tissue phantoms. Troy *et al.* proposed and tested the optical properties of a 2% Intralipid solution across the 400 – 2,200 nm wavelength range [3], and found it closely mimics the optical properties of skin, therefore this phantom composition was used for this study.

3.2.2: Fabrication of Water/Intralipid Phantoms

Intralipid phantoms were fabricated by combining 2% Intralipid and 98% water by weight. The Intralipid stock solution was a 20% emulsion in water (Sigma-Aldrich, I-141). The water content of the stock emulsion was accounted for in the calculations. The solution was poured into 56 mm diameter plastic petri dishes for experiments. The volume required to bring each phantom up to the desired height was determined by assuming the petri dish to be a cylinder and using the dish's radius and the desired height of the phantom to determine the volume of Intralipid solution required.

3.2.3: Experiments with Water/Intralipid Phantoms

For transmission experiments using Intralipid phantoms, the phantom height was adjusted to match the thickness of the silicone phantoms described in Section 3.1.1. The same laser illumination power and camera exposure time (4.69 mW and 0.163 ms respectively) from the transmission experiments with the silicone phantoms with varying thickness was also kept. Matching these parameters allowed for the comparison of the two

data sets and to examine the effects of introducing water to the phantom. Again, it is important to note that transmission images taken at 980 nm were acquired with a 2.36 ms exposure time and the mean pixel intensities were reported following correction to estimate the mean pixel intensity that would have been measured at an exposure time of 0.163 ms. The correction for quantum efficiency discussed in Section 3.1.2 was also applied to the transmission values at 980 nm.

From comparing the transmission experiments of the silicone phantom set with varying thickness and the Intralipid phantom set (**Figure 14** and **Figure 19**) it is apparent that the water based phantoms attenuate more light than the silicone phantoms for each wavelength tested. Contrast measurements for the Intralipid phantoms were performed on thinner phantoms of 1.5 mm, 2.0 mm, 2.5 mm, 3.0 mm, and 3.5 mm to ensure that images had sufficient signal-to-noise ratio to examine contrast. The power and exposure time was adjusted to bring each image to just below saturation.

3.2.4: Results of Experiments with Water / Intralipid Phantoms

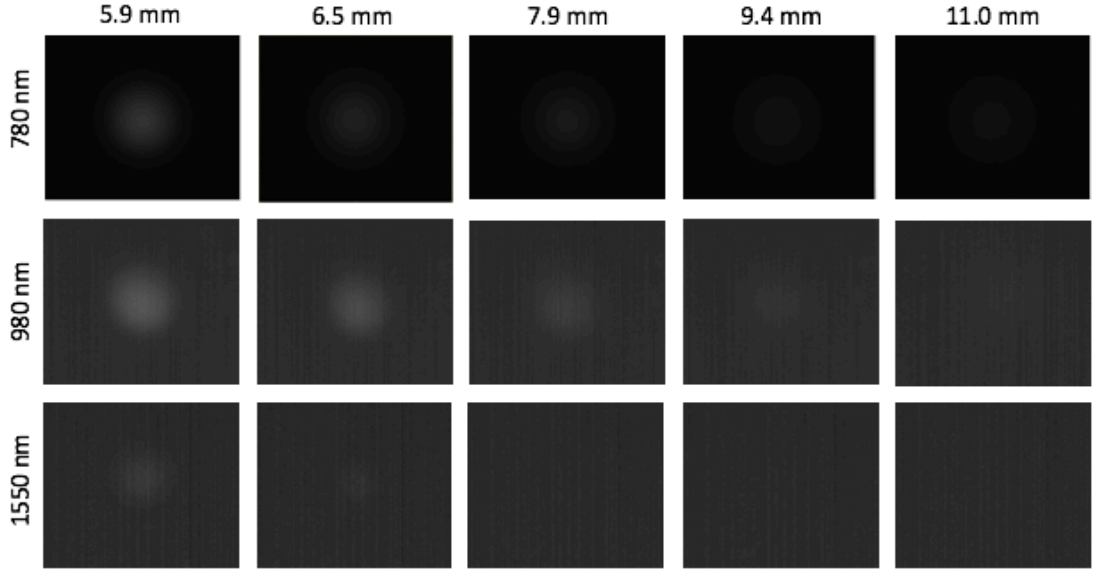

Figure 19: Images obtained from transmission experiments using Intralipid phantoms with varying

thickness. As the thickness of the phantom increases, the amount of light transmitted through the tissue phantom decreases across all wavelengths. All images were taken at a power of 4.69 mW, however, the 780 nm and 1550 nm images were taken at an exposure time of 0.163 ms, while the 980 images were taken at an exposure time of 2.36 ms.

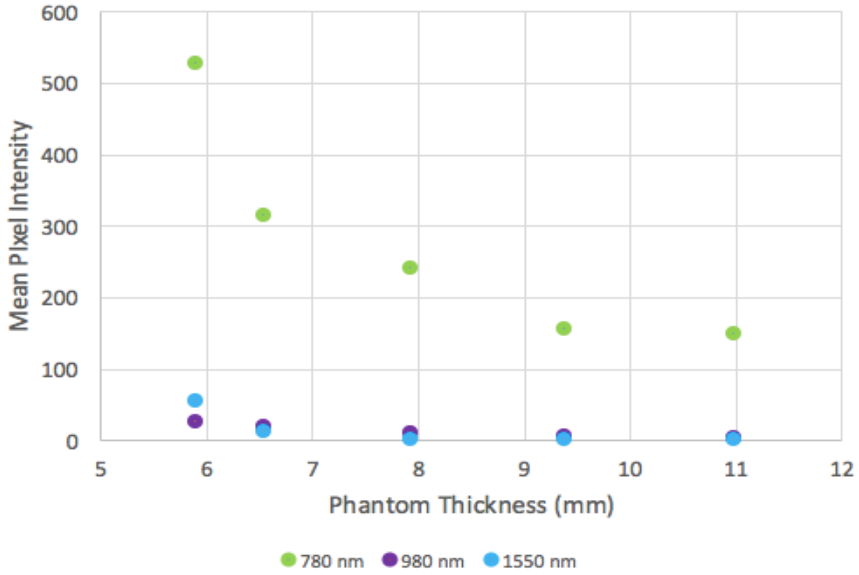

Figure 20: Plot of the transmission of light at 780 nm, 980 nm, and 1550 nm wavelengths through Intralipid phantoms. The mean pixel intensity values reported at 980 nm have been corrected for camera exposure time and quantum efficiency.

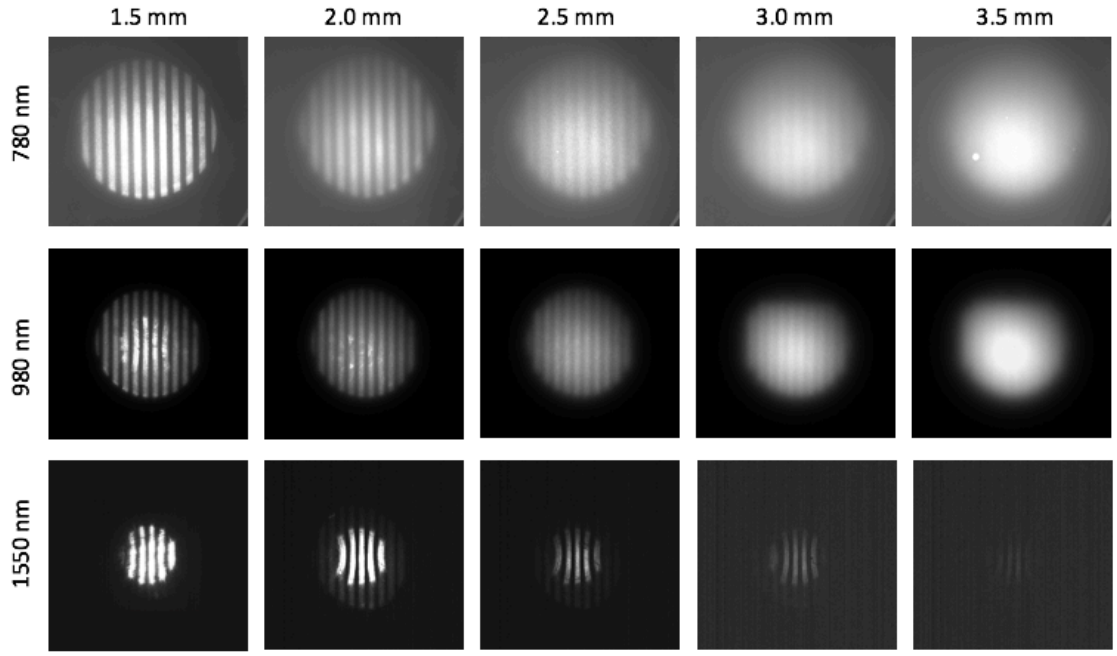

Figure 21: Imaging a Ronchi grating through 2% Intralipid phantoms of varying thickness. As the thickness of Intralipid solution increases, the contrast that can be obtained decreases for all wavelengths tested. However, the 1550 nm wavelength appears to provide the highest contrast at each thickness tested.

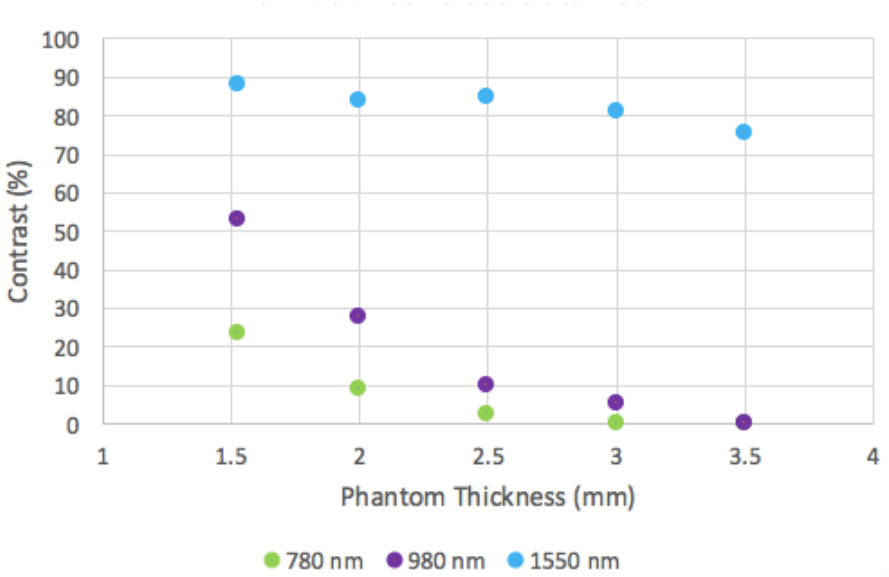

Figure 22: Plot of the maximum image contrast obtained for Intralipid phantoms at 780 nm, 980 nm, and 1550 nm wavelengths. The 1550 nm wavelength provided images with the highest contrast for all thicknesses tested.

3.3: DISCUSSION

When examining the transmission results shown in **Figures 11, 15, and 19** it is important to note that the 780 nm wavelength images were taken on a silicon camera while the 980 nm and 1550 nm images were taken on an InGaAs camera**.** All auto-adjustment and background settings were turned off and incident laser power levels and exposure times were matched, however, there will still be differences as the cameras have a different sensitivity to incident light. For this reason, we cannot make a definitive conclusion about the absolute intensities of NIR wavelengths versus SWIR wavelengths on propagation through tissue. However, we can state some conclusions about which wavelengths can be imaged more easily, given the camera technology available.

3.3.1: Discussion of Silicone Phantom Results

Phantom	Wavelength (nm)	Scattering Coefficient (1/mm)	Silicone Absorption Coefficient (1/mm)	Transport Mean Free Path (mm)
0.03 g	780	0.32	0.0006	3.12
	980	0.25	0.0008	3.99
	1550	0.15	0.05	5
0.04 g	780	0.49	0.0006	2.04
	980	0.38	0.0008	2.63
	1550	0.23	0.05	3.57
0.06g	780	0.89	0.0006	1.12
	980	0.73	0.0008	1.37
	1550	0.5	0.05	1.82
0.08g	780	1.07	0.0006	0.93
	980	0.88	0.0008	1.14
	1550	0.62	0.05	1.49
0.09g	780	1.29	0.0006	0.77
	980	1.09	0.0008	0.92
	1550	0.82	0.05	1.15

Table 2: A table displaying the scattering coefficients, absorption coefficients, and transport mean free paths for the silicone phantoms with varying amounts of TiO. The silicon phantom set that varies in thickness has the same optical properties as the phantom with 0.06g of TiO. The scattering coefficients are as shown in **Figure 9**. The coefficient at 780 nm was interpolated from the SDFI data while the coefficients at 980 nm and 1550 nm were extrapolated. The absorption coefficient listed in the table has been approximated from the plot in **Figure 18** as silicone can be assumed to be the main absorbing agent because its concentration is much higher than that of the nigrosin. Transport free path was calculated using the formula: TMFP = $1/(\mu_a+\mu'_s)$.

From the transmission experiments performed on the silicone phantoms with varying amounts of TiO (**Figure 11)**, it appears that the 1550 nm wavelength propagates through the silicone phantoms with lower attenuation than the 980 nm wavelength, regardless of the amount of TiO present. The scattering and absorption coefficients in **Table 2** support these findings. We can see that even though the silicone matrix has a much higher absorption at 1550 nm than 980 nm, propagation of light through these phantoms is dominated by the much larger scattering coefficients, which are lower at 1550 nm than 980 nm. The 780 nm wavelength appears to have a higher transmission signal through the phantoms than the 980 nm wavelength for all amounts of TiO, even though this wavelength has the highest scattering coefficient for each phantom. However, as discussed earlier, this

observation is likely to be due to internal differences between the silicon camera used for 780 nm imaging, and the InGaAs camera used for 980 nm and 1550 nm.

A look at the transmission results from the silicone phantom set of varying thicknesses, displayed in **Figure 15** reveals a similar trend as the phantom set with varying amounts of TiO (**Figure 13**). As thickness increases, the transmission of the 1550 nm wavelength decreases much faster than the transmission of the 980 nm wavelength. It appears that for thinner phantoms, the 780 nm wavelength had a lower transmission signal than the 1550 nm wavelength. However, as thickness increases, 780 nm transmitted the farthest through the silicone phantoms.

Examination of the contrast results for both silicone phantom sets, depicted in **Figures 13** and **17**, reveals the same trend. A much higher contrast was observed at the longer SWIR wavelengths, regardless of the scattering properties of the phantom or phantom thickness. As the scattering coefficient of the wavelength decreased, the image contrast increased. 780 nm, which has the highest scattering coefficient of the three wavelengths tested, offered the lowest contrast images, while 1550 nm, which has the lowest scattering coefficient of the wavelengths, provided the highest contrast images. Using a wavelength with a lower reduced scattering coefficient allows more of the photons to remain in the ballistic regime [5]. As ballistic photons are not scattered they propagate along their trajectory, preserving image resolution.

3.3.2: Discussion of Water/Intralipid Phantom Results

Wavelength (nm)	Reduced Scattering Coefficient (1/mm)	Intralipid Absorption Coefficient (1/mm)	Transport Mean Free Path (mm)
780	2.05	0.0026	0.49
980	1.58	0.047	0.61
1550	1.52	1.9	0.29

Table 3: Reduced scattering coefficients, absorption coefficients, and transport mean free paths for the Intralipid phantoms. The coefficients for 780 nm and 980 nm were calculated using the Virtual Photonics simulator, while the coefficients for the Intralipid phantoms at 1550 nm were found in reference [6].

An important observation from comparing the results of the transmission experiments from the silicone phantom set of varying thickness to the Intralipid phantom set is that the Intralipid set had a much lower transmission due to the introduction of water. Water has a very high absorption, especially in the SWIR region and results from the Intralipid phantom set reflect this.

From the transmission results displayed in **Figure 20**, it is evident that the 780 nm wavelength appears to have the highest transmission through the Intralipid phantoms. As seen in **Table 3**, the transport mean free path at 980 nm is highest implying that 980 nm should have the highest transmission since fewer photons are diffuse. Another reason for these results could be that the silicon camera is simply better at detecting low levels of light.

An examination of the contrast experiments displayed in **Figure 22** shows that again, 1550 nm offers the best image contrast. The lower scattering coefficient of the wavelengths in the SWIR region means that fewer photons enter the diffuse regime [5].

Based on the above experiments and discussion, a wavelength in the NIR spectrum or SWIR spectrum should be chosen with the application in mind. As 780 nm seems to be most readily detected, it may be best to choose a NIR wavelength for an application that

purely requires detection of light. However, as the 1550 nm appears to provide the best overall image contrast, for applications that require resolving tissue features, a SWIR wavelength may be the best option.

3.4: REFERENCES

1. Agrawal, A., *et al*. “Characterizing the Point Spread Function of Retinal OCT Devices with a Model Eye-Based Phantom.” *Biomedical Optics Express*, 2011.
2. Balter, M., *et. al.* “Adaptive Kinematic Control of a Robotic Venipuncture Device Based on Stereo Vision, Ultrasound, and Force Guidance.” *IEEE Transactions on Industrial Electronics*, vol. 64, no. 2, 2017, p. 1626-1635.
3. Bashkatov, A., *et al*. “Optical Properties of Human Skin, Subcutaneous and Mucous Tissues in the Wavelength Range from 400 to 2000 nm.” *Journal of Physics D: Applied Physics*, vol. 38, no. 15, 2005, p. 2543–2555.
4. Cubeddu, R., *et. al*. “A Solid Tissue Phantom for Photon Migration Studies.” *Physics in Medicine and Biology*, vol. 42, no. 10, 1997, p. 1971-1979.
5. Sordillo L., *et.al*. “Deep Optical Imaging of Tissue Using the Second and Third Near-Infrared Spectral Windows.” *Journal of Biomedical Optics*, vol. 19, no. 5, 2014.
6. Troy, T., *et al.* “Optical Properties of Human Skin in the Near Infrared Wavelength Range of 1000 to 2200 nm.” *Journal of Biomedical Optics*, vol. 6, no. 2, 2001, p. 167-176.
7. Ntziachristos, V. “Going Deeper Than Microscopy: The Optical Imaging Frontier in Biology.” *Nature Methods*, vol. 7, no. 8, 2010, p. 603–614.

CHAPTER 4: EXPERIMENTS USING BIOLOGICAL TISSUE

Although the phantoms used in Chapter 3 can simulate the propagation of light through tissue, they fail to mimic some properties of biological tissue. Phantoms have a uniform composition while tissue is not uniform. Changes in tissue microstructure caused by cellular arrangement and inhomogeneous composition effect the behavior of light propagating through it. Another drawback of the solid and liquid phantoms used earlier is the lack of true biological components. Tissue contains many components including blood, lipid, collagen, melanin, and others, each of which contribute to the overall scattering and absorbing properties. For these reasons, in order to gain the best understanding of light propagation *in vivo*, the experiments described in Chapter 3 were repeated with *ex vivo* tissue. Chicken tissue was chosen because it was easy to obtain and had been utilized in previous studies [3]. As tissue morphology and composition varies depending on tissue type [1], two different tissues were tested, chicken breast tissue and chicken liver tissue. Breast tissue contains little to no blood, while liver tissue has higher blood content.

4.1: CHICKEN BREAST

4.1.1: Experiments with Chicken Breast – Methods

The transmission and contrast experiments described in Chapter 2 were performed on chicken breast tissue. Three different thicknesses of tissue were tested: 2 mm, 4 mm, and 6 mm. For the transmission experiments, a laser power of 6.5 mW and a camera exposure time of 2.36 ms was selected, based on earlier results in Intralipid phantoms. For the contrast experiments, the incident laser power and the camera exposure times were adjusted for each phantom at each wavelength to yield the highest contrast. As the goal of the contrast experiments was to see which wavelength could provide the highest contrast

imaging through tissue, it was not necessary for laser power levels and camera exposure times to mirror each other.

4.1.2: Experiments with Chicken Breast – Results

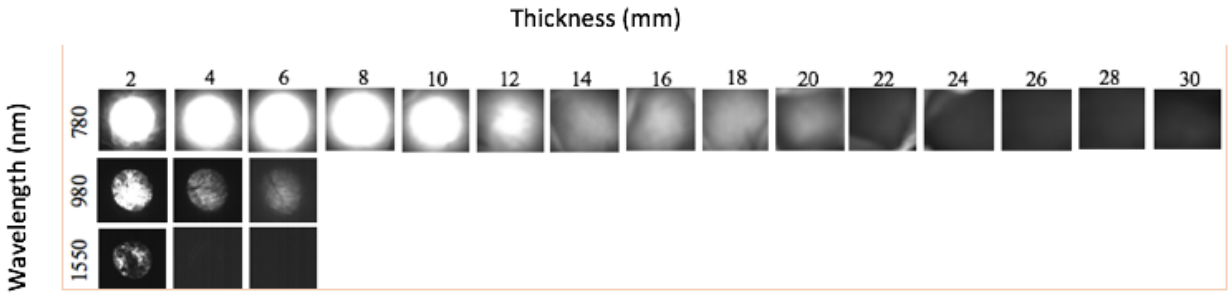

Figure 23: Images obtained from transmission experiments in chicken breast tissue. As the thickness of tissue increases, the amount of transmitted light decreases for each wavelength tested. All images were taken with an incident laser power of 6.5 mW and a camera exposure time of 2.36 ms.

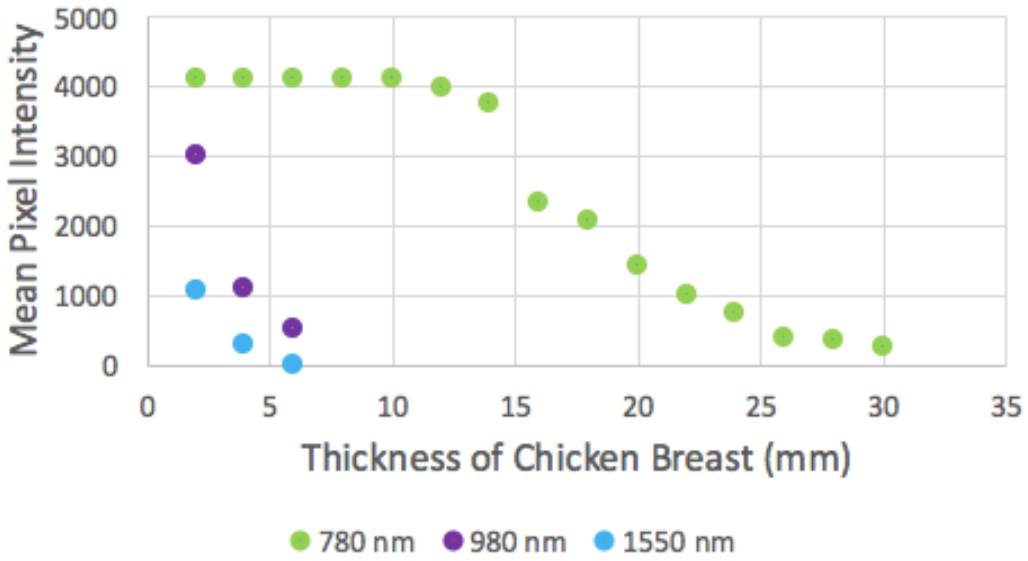

Figure 24: Plot of the mean pixel intensity in a region-of-interest in images shown in **Fig. 23**, for 780 nm, 980 nm, and 1550 nm wavelengths through chicken breast tissue. As the thickness of the tissue increases, the measured mean pixel intensity decreases across all wavelengths.

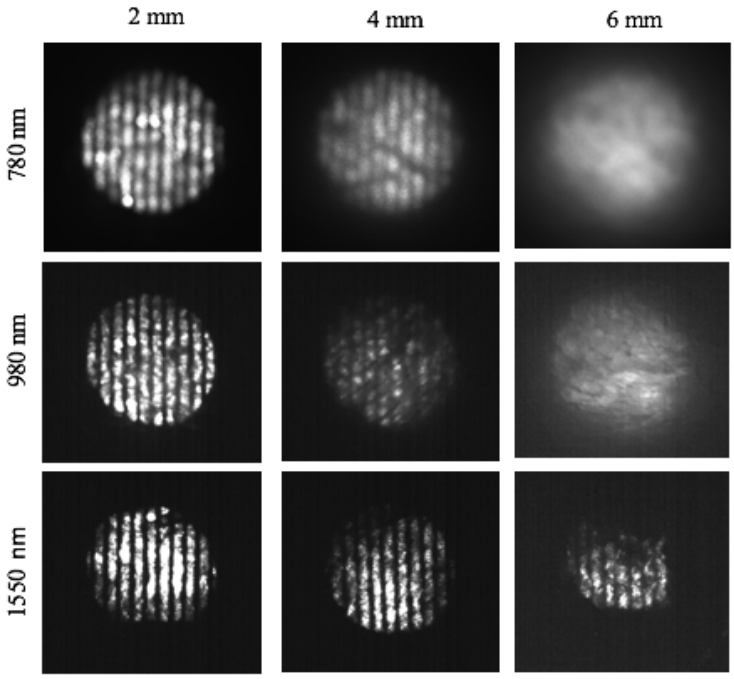

Figure 25: Images obtained from the contrast experiments with chicken breast tissue. As tissue thickness increased, the contrast that could be obtained decreased for all wavelengths. Imaging at 1550 nm appears to provide images with the highest contrast

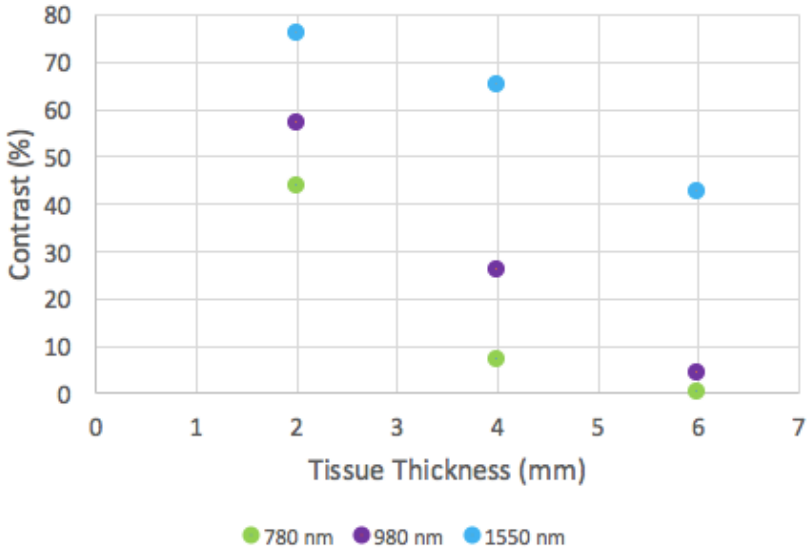

Figure 26: Plot of the maximum image contrast obtained for chicken breast tissue at 780 nm, 980 nm, and 1550 nm. 1550 nm provides images with the highest contrast, at all thicknesses tested.

4.2: CHICKEN LIVER

Chicken liver was studied as it has a higher blood content than chicken breast, which may affect transmission and / or contrast.

4.2.1: Experiments with Chicken Liver - Methods

Three different tissue thicknesses were tested: 2 mm, 4 mm, and 6 mm. For transmission experiments, the initial goal was to keep the laser power level and camera exposure time the same as used previously in the experiments with the chicken breast in order to compare the two sets of tissues. However, it quickly became apparent that the liver tissue was more highly attenuating than the chicken breast tissue and maintaining the same laser power and camera settings would result in images with low signal to background levels. Therefore, the 980 nm laser was used with the thinnest (2 mm) sample to determine a new combination of laser power and camera exposure time that generated images just below saturation for the liver tissue. The laser power and camera exposure time selected for liver tissue were 10.9 mW and 2.36 ms, respectively. Once again, the 780 nm images of the thinner tissue samples were saturated but tissue slices were added until the signal became too weak to detect. For the contrast experiments, the incident laser power and the camera exposure times were again adjusted for each phantom at each wavelength to yield the highest contrast.

4.2.2: Experiments with Chicken Liver – Results

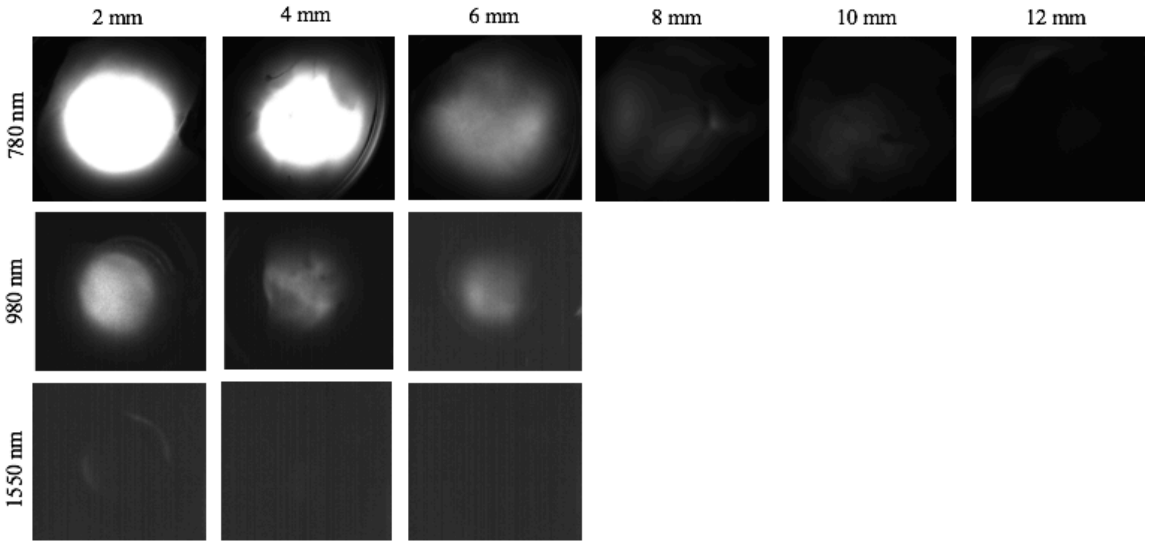

Figure 27: Images obtained from transmission experiments in chicken liver tissue. As the thickness of tissue increases, the amount of light transmitted decreases across all wavelengths. All images were taken with an incident laser power of 10.9 mW and a camera exposure time of 2.36 ms.

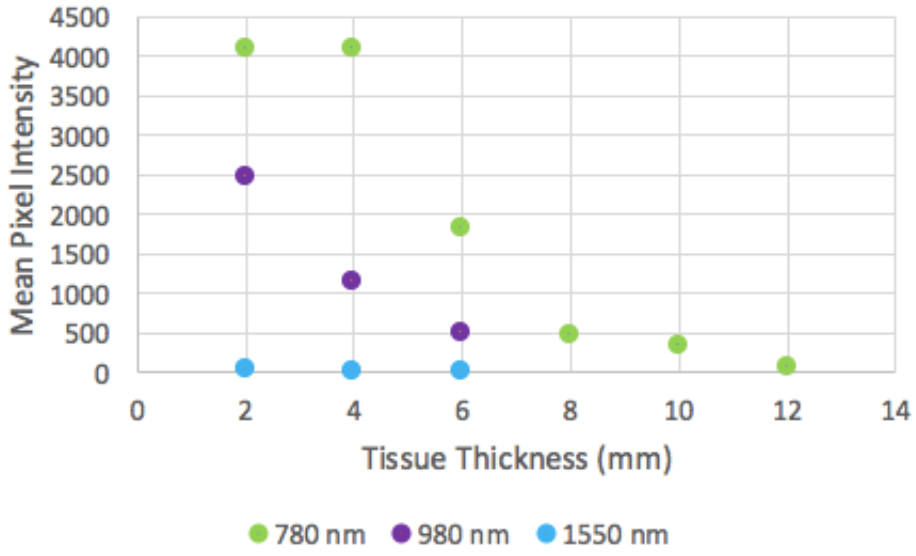

Figure 28: Plot of the mean pixel intensity within a region-of-interest in the transmission images shown in **Fig. 27**, using 780 nm, 980 nm, and 1550 nm wavelengths and chicken liver tissue. As the thickness of the tissue increases, the measured mean pixel intensity decreases across all wavelengths.

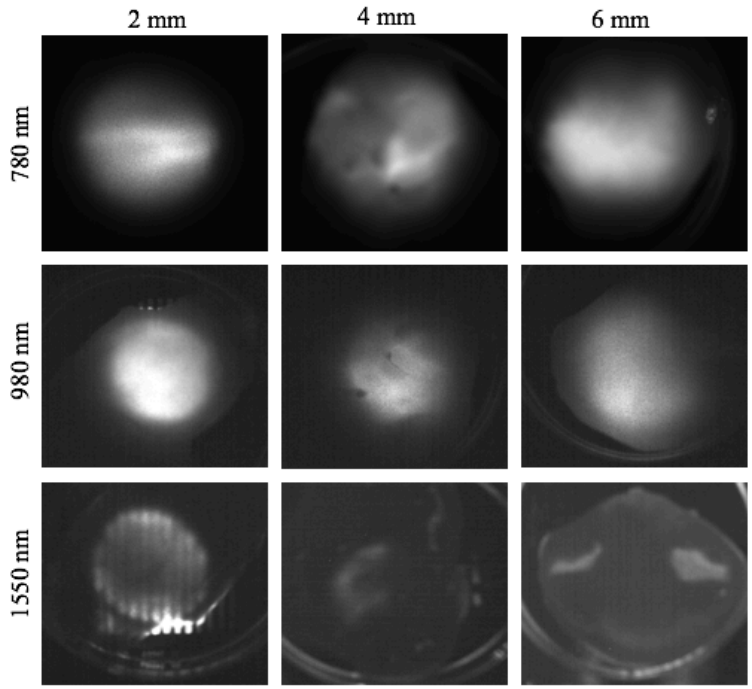

Figure 29: Images obtained from contrast experiments with chicken liver tissue. As tissue thickness increased, the contrast that could be obtained decreased at all wavelengths tested. Imaging at 1550 nm appears to provide images with the best contrast. Images at 1550 nm were taken at a much higher laser power and camera exposure time than the 780 nm and 980 nm images in an attempt to view the Ronchi grating under the tissue.

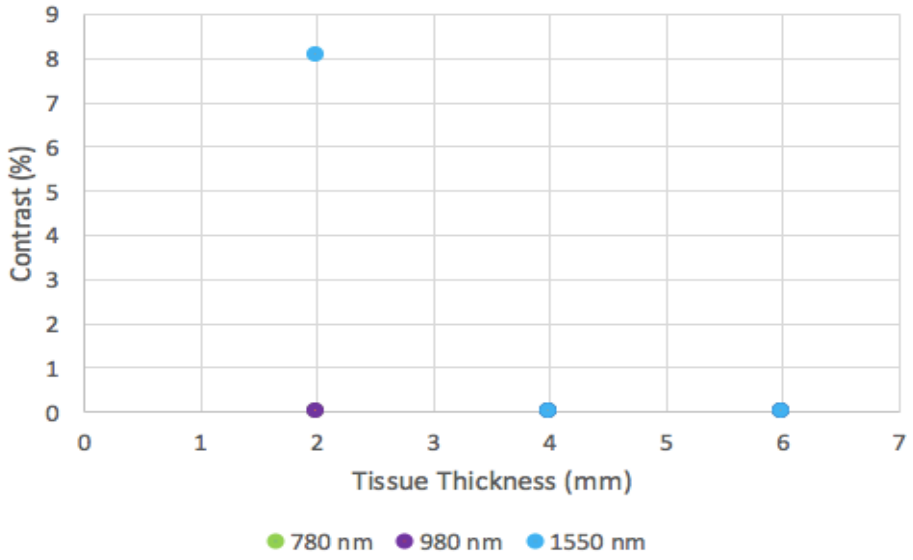

Figure 30: Plot of the maximum image contrast obtained for chicken liver tissue at 780 nm, 980 nm, and 1550 nm. 1550 nm provides images with the highest contrast, for all thicknesses. The 780 nm markers are overlapping with the 980 nm points, corresponding to 0% contrast at each of these wavelengths.

4.3: DISCUSSION

	Wavelength (nm)	Reduced Scattering Coefficient (1/mm)	Absorption Coefficient (1/mm)	Transport Mean Free Path (mm)
Breast Tissue	780	0.848	0.00589	1.18
	980	0.683	0.0226	1.46
Liver Tissue	780	0.963	0.039	1.04
	980	0.849	0.0796	1.18
Skin	780	1.71	0.0873	0.56
	980	1.23	0.0757	0.76
	1550	1	0.8	0.55

Table 4: Table displaying the reduced scattering coefficient, absorption coefficient, and predicted transport mean free path at 780 nm, 980 nm, and 1550 nm wavelengths for breast tissue, liver tissue and skin. Scattering and absorption coefficients for 780 nm and 980 nm are from the Virtual Photonics Simulation website and the reduced scattering coefficient and absorption coefficient at 1550 nm were taken from Troy *et. al.* [4]. Transport mean free path was calculated using the $1/(\mu_s' + \mu_a)$ formula.

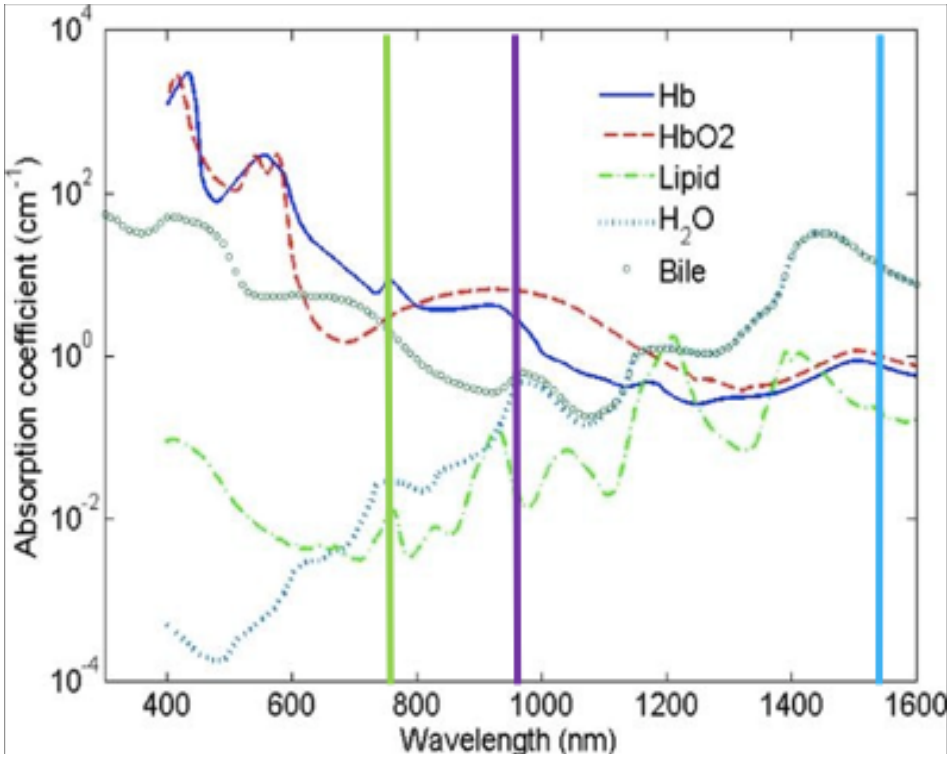

Figure 31: Absorption spectra of several major components of tissue [2]. Wavelengths of 780 nm, 980 nm, and 1550 nm have been marked in green, purple, and blue respectively.

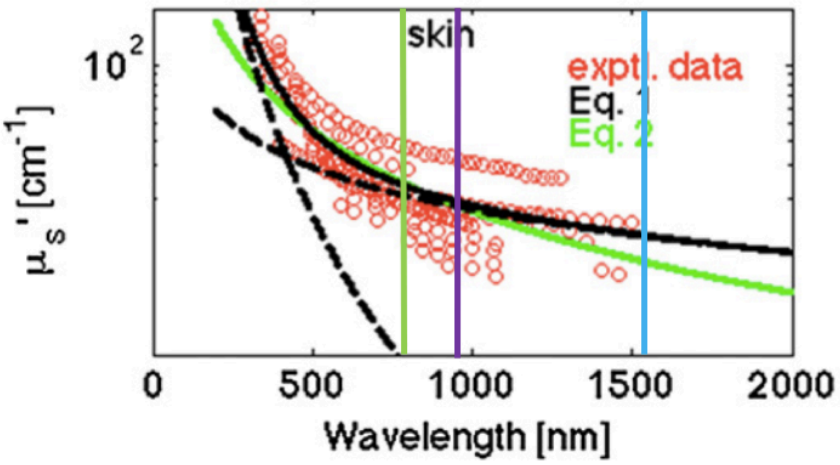

Figure 32: Scattering spectra of skin [1]. 780 nm, 980 nm, and 1550 nm wavelengths have been marked with green, purple, and blue lines, respectively.

From the transmission experiments performed on both the chicken breast tissue and the chicken liver tissue, the 780 nm wavelength appears to exhibit the highest mean pixel intensity values in the acquired images (**Figures 24** and **28**) and the 980 nm wavelength appears to propagate through tissue with less attenuation than 1550 nm. Again, it is possible that the silicon camera is simply more sensitive to low levels of NIR light than the InGaAs camera in the SWIR region.

Examining the absorption coefficients in **Table 4** and the absorption spectra displayed in **Figure 31** appears to offer an explanation as to why the results are as is. The coefficients for 780 nm and 980 nm were obtained from the Virtual Photonics website, http://www.virtualphotonics.org/vts/. As Virtual Photonics only provides optical property data for wavelengths up to 1000 nm, a different source had to be utilized to obtain the scattering and absorption coefficients at 1550 nm. Relatively few studies have been conducted to measure tissue optical properties in the shortwave infrared region, therefore the reduced scattering and absorption coefficients for breast and liver tissue at 1550 nm

were not available. However, the reduced scattering and absorption coefficient at 1550 nm for skin was found in a study by Troy *et. al* [4]. Although skin was not one of the tissues measured in this thesis, the availability of optical property values from the literature allow for an approximate comparison to liver tissue and breast tissue to be made. From **Table 4,** it is evident that the longer wavelengths have a higher absorption coefficient and **Figure 31** shows this increase is due to the water content. As wavelength increases, the absorption coefficient of water also increases. It is the increased attenuation of water at the longer wavelengths that is contributing to the decrease in transmission at the longer wavelengths.

Liver tissue had much lower mean pixel intensity measurements than breast tissue despite the increase in incident laser power. This can also be attributed to the absorption coefficient of liver being higher than that of breast tissue at 780 nm and 980 nm (**Table 4)**. This could be because of the additional blood content in liver, which contributes more to absorption at these wavelengths than water (**Figure 31**). A related observation is the significant decline in transmission at 780 nm between breast tissue and liver tissue. Despite using a higher incident laser power level for liver tissue, 780 nm light was only measurable through about 12 mm of liver tissue while it propagated through about 30 mm of breast tissue. This can again be attributed to the presence of blood in liver tissue. As water's absorption at 780 nm is low and breast tissue is primarily water, the 780 nm light propagated through breast tissue with relatively low attenuation. However, at 780 nm blood does impact absorption, and since the liver tissue contained blood the 780 nm wavelength experienced more attenuation while propagating through the liver tissue.

From the contrast experiments (**Figures 26** and **30**) it is evident that the 1550 nm wavelength offers the best contrast for imaging through both breast and liver tissue. As

shown in **Figure 32**, the reduced scattering coefficient for tissue declines as wavelength increases. As the scattering coefficient is lower at 1550 nm, more photons remain in the ballistic regime while travelling through tissue, preserving image contrast. Resolving the Ronchi grating through liver tissue was particularly difficult as attenuation was very high. Despite using about 45 mW of power, (the maximum output available on the device used) obtaining good contrast results was not possible.

From the experiments performed above, it is apparent that the wavelength of choice should be selected with the application specific purpose in mind. If the goal is simply detection of signal, then a NIR wavelength should be chosen. If the goal is to resolve structure within tissues, then a SWIR wavelength should be selected as the 1550 nm wavelength provided the best contrast through both types of tissues.

4.4: REFERENCES

1. Jacques, S. “Optical Properties of Biological Tissues: A Review.” *Physics in Medicine and Biology*, vol. 58, no. 11, 27 June 2013, p. 37-61.
2. Nachabé R., *el al.* “Estimation of Biological Chromophores Using Diffuse Optical Spectroscopy: Benefit of Extending the UV-VIS Wavelength Range to Include 1000 to 1600 nm.” *Biomedical Optics Express*, vol. 1, no. 5, 2010, p. 1432-1442.
3. Sordillo, L., *et al*. “Deep Optical Imaging of Tissue Using the Second and Third near-Infrared Spectral Windows.” *Journal of Biomedical Optics*, vol. 19, no. 5, 2014.
4. Troy, T., *et al.* “Optical Properties of Human Skin in the Near Infrared Wavelength Range of 1000 to 2200 nm.” *Journal of Biomedical Optics*, vol. 6, no. 2, 2001, p. 167-176.

CHAPTER 5: DISCUSSION

5.1: DISCUSSION OF RESULTS

From the experiments performed in Chapters 3 and 4 with the tissue simulating phantoms and *ex vivo* chicken tissue the following conclusions can be drawn. Given the current technology available on the market, for an application that aims to detect a signal from labeled tissue, nanoprobes that emit NIR wavelengths should be utilized. In the transmission experiments performed, the 780 nm wavelength was imaged with higher signal to background levels than 980 nm and 1550 nm, through both tissue simulating phantoms and biological tissue. It was previously thought by Naczynski *et. al.* that the lower scattering coefficients experienced by longer wavelengths would compensate for the increased absorption by water, allowing for greater transmission through tissue. This may indeed be true, but when we take into account the capability of current state-of-the-art cameras for imaging at these wavelengths, we find that NIR wavelengths are more readily detected than SWIR light, given the currently available camera technology.

For applications aiming to resolve the structural details of tissue labeled by fluorescent probes, materials that emit in the SWIR region should be utilized. From the contrast experiments performed in Chapter 3 and 4 on both the tissue simulating phantoms and real tissue it is apparent that the 1550 nm wavelength offered the best image contrast. At longer wavelengths, the scattering coefficient of the wavelength decreases, allowing for increased image contrast.

5.2: SUGGESTIONS FOR FUTURE WORK

5.2.1: Introduction

The rare earth doped nanoparticles under study are unique because they have dual emission capabilities, producing wavelengths in both the visible spectrum and the SWIR region upon excitation from a single 980 nm source. What remains to be studied are the available practical applications of this dual emission. One application that has been under study is the possibility to use multicolor imaging methods to image several different types of lesions with the excitation of one nanoparticle [2].

Another possible application under examination is optogenetics. Optogenetics involves genetically modifying cells to express light-activated proteins. Using optogenetic techniques, the excitation, inhibition, or signaling pathways of cells can be controlled [3]. Most currently used optogenetic proteins are activated by visible light. However, delivering visible light to modified cells deep within tissue can be difficult as visible light has a very low penetration depth in tissue. Currently, a fiber-optic probe must be inserted in order to deliver the visible light necessary for activating optogenetic proteins deep in tissue. Some disadvantages to this technique are tissue infections and constraint of movement when implanted for long term *in vivo* experiments in animals [5]. For this purpose, there has been a search for an alternative method to deliver the visible light. Recent studies have focused on using the visible emissions produced by the excitation of rare-earth doped nanoparticles to activate the optogenetic proteins. As the studies conducted in this thesis found SWIR wavelengths to be the best for resolving tissue, the visible wavelengths emitted from the rare-earth nanoparticles used to produce these SWIR emissions can be used to simultaneously activate optogenetic proteins, performing two functions with one excitation [1].

An alternate potential application of the dual wavelength emission is to determine the depth of the nanoprobe labeled cells, as discussed in Liu *et al*. [2]. With conventional 2D imaging, it is difficult to determine a lesion's depth in tissue. A possible way to determine the depth of a lesion labeled with rare-earth doped nanoprobes is by calculating the ratio between the detected visible light and the detected SWIR emission. This ratio will vary with nanoprobe depth due to the difference in propagation of light at visible and SWIR wavelengths. Visible wavelengths experience more attenuation while propagating through tissue than SWIR wavelengths. For this reason, as nanoprobe depth increases, the ratio of the measured SWIR emission signal to the visible light signal will increase. If this relationship can be determined or calibrated for specific tissue types, then it may be possible to infer nanoprobe depth from measurements of SWIR : visible emission signal.

5.2.2: Determining Nanoprobe Depth in Tissue

A pilot experiment was performed to assess the feasibility of determining nanoprobe depth beneath tissue simulating phantoms.

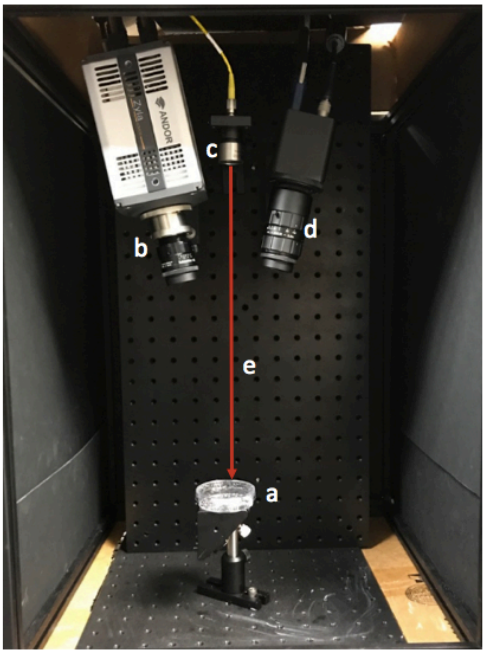

Figure 33: The set-up used to image visible and SWIR wavelength emissions from rare-earth-doped nanoparticles. A 980 nm collimated beam was used to excite the nanoparticles, while the silicon camera and the InGaAs camera simultaneously captured emissions. **(**a) Nanoparticles (b) silicon camera (c) 980 nm collimated beam (d) InGaAs camera. The setup was enclosed in a light tight box.

The experimental set-up is shown in **Figure 33**. A sample of dry nanoprobes was placed into a plastic petri dish and silicone phantoms of varying thickness (0.4 mm, 0.5 mm, 0.8 mm, 0.9 mm, 1.2 mm, and 1.3 mm) were placed on top. Light from the 980 nm laser was collimated (Thorlabs, F810FC-1064) and passed through the silicone tissue phantoms to excite the nanoparticles. Both the silicon camera (Andor, Zyla 5.5 sCMOS) and the InGaAs (Sensors Unlimited, GA1280JS) camera were utilized to simultaneously detect nanoprobe emissions. To ensure that the cameras did not detect the 980 nm excitation wavelength, filters were placed on both camera lenses. A 694 nm shortpass filter (Semrock, FF02-694/SP-25) was placed onto the silicon camera lens, while a 980 nm longpass filter (Semrock, BLP01-980R-25) was placed onto the InGaAs camera lens. As the ambient light

contains wavelengths below 700 nm, the set-up was placed inside a dark box to ensure the silicon camera did not also pick up the room light.

The nanoprobes tested were optimized to emit in the SWIR wavelength region and initial tests confirmed that the nanoprobes were producing much less visible light than shortwave infrared light. Using the same laser power and camera exposure time produced a saturated SWIR image on the InGaAs camera while the visible emission was barely detected on the silicon camera. It should be noted that the pixel size of the silicon camera is 6.5 μm x 6.5 μm while the pixel size of the InGaAs camera is 12.5μm x 12.5 μm. This indicates that one of the factors contributing to weaker signal on the silicon camera is the smaller light collection area per pixel.

For subsequent experiments, pixel binning settings and camera exposure times that optimized image quality were selected. Binning, while combining multiple pixels into one pixel in order to provide a greater area to collect light, leads to a loss of image resolution. 4 x 4 pixel binning was used in this experiment. The 980 nm laser power was set to 7.2 mW and the thinnest silicone phantom (0.4 mm) was placed over the nanoprobes. The camera exposure times were set on each camera so that the images detected were just below saturation. The silicon camera was set to an exposure time of 1.2 s while the InGaAs camera was set to an exposure time of 2.36 ms.

A region of interest encompassing the incident beam was defined within the acquisition and analysis software for each camera and the mean pixel intensity within this region was recorded as phantoms of increasing thickness were placed over the nanoprobe sample. The background level of each camera was also determined by recording the mean pixel intensity while the lens covers were on the cameras. These values were subtracted

from the mean pixel intensities recorded. The background-corrected mean pixel intensity detected by the InGaAs camera was divided by the mean pixel intensity detected by the silicon camera for each phantom thickness in order to determine the emission ratio.

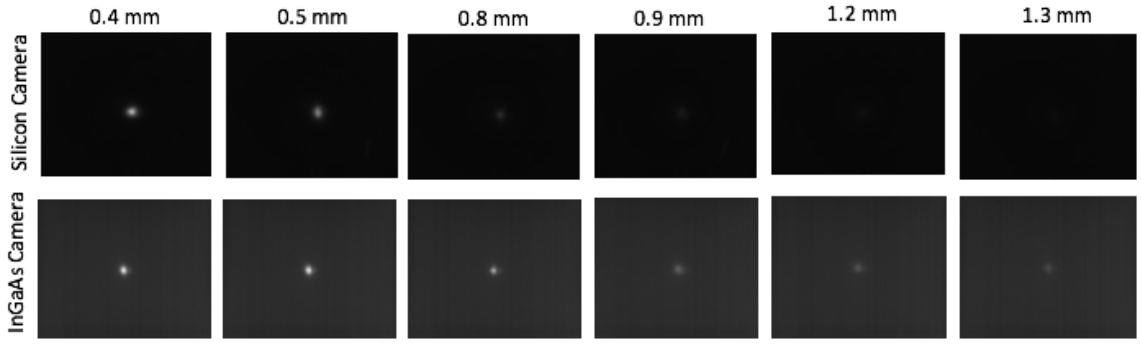

Figure 34: Images obtained from the dual wavelength detection experiment. It is evident that the signal that the silicon camera detects diminishes faster than the signal detected by the InGaAs camera as tissue phantom thickness increases, despite the application of a binning setting (4 x 4) and a longer exposure time. A 980 nm laser power of 7.2 mW was used. The silicon camera had an exposure time of 1.2 s, while the exposure time for the InGaAs camera was set to 2.36 ms.

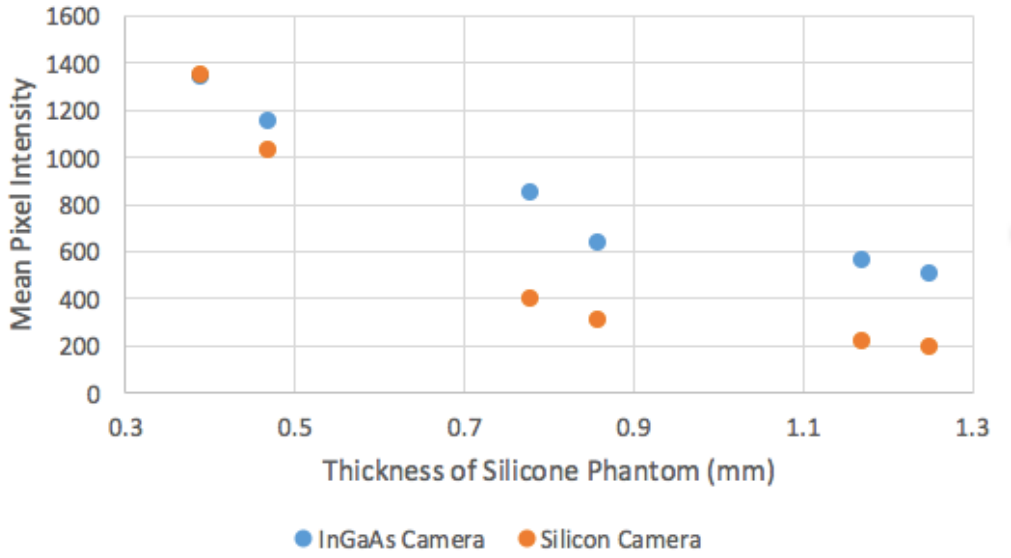

Figure 35: Plot of the mean pixel intensities recorded on both cameras at each thickness. As phantom thickness increases, the mean pixel intensity detected by the silicon camera decreases faster.

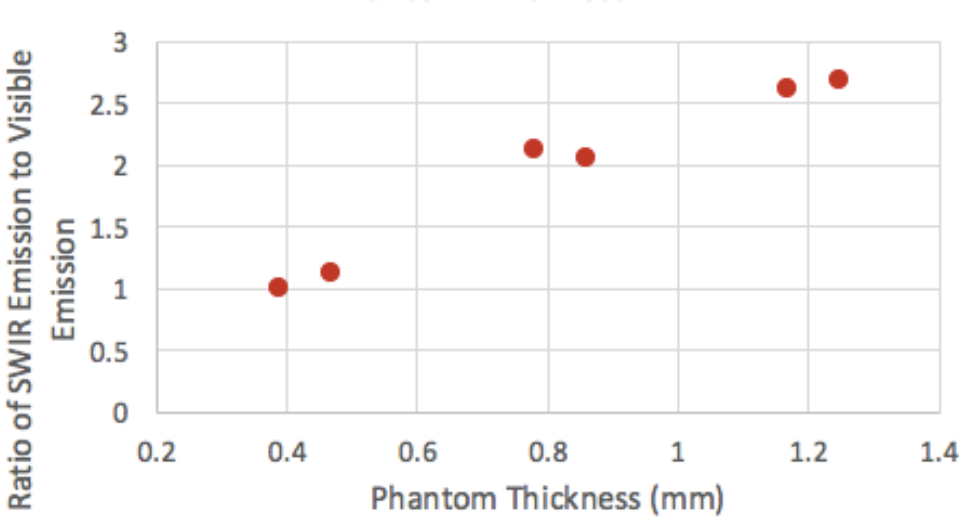

Figure 36: Plot of ratios of shortwave infrared emission to visible emission versus phantom thickness. It appears that the ratio increases as the phantom thickness increases.

It appears that the ratio of SWIR emissions to visible light emissions is dependent on the depth of the luminescent nanoprobe within tissue. From **Figure 36** it is evident that the SWIR to visible emission ratio increases with increasing phantom thickness. As phantom depth increases, the visible wavelength signal experiences more attenuation than the SWIR wavelengths, thus increasing the emission ratio. Provided each camera setting used for depth estimation is the same as that used for calibrating the ratios for each depth, it does appear that the depth can be determined if the ratio of the emissions is known. While **Figure 36** shows that the change in ratio from one depth to the next is very small, it is important to note that the difference in the tissue depths tested was also very small.

5.3: SUMMARY AND CONCLUSION

This work focused on performing transmission and contrast experiments on both tissue simulating phantoms and biological tissues to examine and compare the behavior of NIR and SWIR wavelengths as they propagate through tissue. Given the results, some

conclusions can be drawn about which wavelength region is ideal for a given practical application, considering the current technology on the market. For an application that is only interested in the detection of signal, NIR wavelengths should be used as cameras available for this wavelength range are more capable of detecting weak signals. For an application that focuses on resolving fine structures of labeled tissues, SWIR wavelengths should be utilized as the reduced scattering of tissue in this region provides better image contrast.

One limitation to the transmission studies was the missing measurement or calculation of the actual intensity of the beam that was transmitted through the tissue simulating phantoms and the biological tissue. By knowing the intensity of the beam that excited the phantom, it could be determined whether the NIR wavelength beam was really transmitted through the medium with less attenuation, or whether the measured SNR was due to improved performance of the silicon sensor, compared to the InGaAs camera. Although these results would not have made a difference in the short term conclusions, they will make a difference once SWIR sensor technology catches up to visible light sensor technology.

The dual emission properties of the nanoprobes under study offer many possibilities for future studies. As demonstrated by the pilot study in Section 5.2.2, it appears to be possible to use the ratio of SWIR emissions to visible emissions to determine nanoprobe depth within tissue. As this method could prove to be a valuable tool for lesion depth determination and lesion depth is necessary for diagnosing cancer stage and forming a prognosis [5], it is recommended that further studies are conducted on this topic.

5.4: REFERENCES

1. He, L. *et al.*, “Near-Infrared Photoactivatable Control of Ca^{2+} Signaling and Optogenetic Immunomodulation,” *eLife*, vol. 4, 2015, p. e10024.
2. Liu, K. *et al.*, “Multispectral Upconversion Luminescence Intensity Ratios for Ascertaining the Tissue Imaging Depth.” *Nanoscale*, vol. 6, 2014, p. 9257–9263.
3. Fenno, L. *et al.*, “The Development and Application of Optogenetics.” *Annual Review of Neuroscience*, vol. 34, 2011.
4. Sordillo, L. *et al*. “Deep Optical Imaging of Tissue Using the Second and Third near-Infrared Spectral Windows.” *Journal of Biomedical Optics*, vol. 19, no. 5, 2014.
5. Wu, X. *et al.* “Dye-Sensitized Core/Active Shell Upconversion Nanoparticles for Optogenetics and Bioimaging Applications.” *ACS Nano*, vol. 10, no. 1, 2016, p. 1060–1066.